Research Square

Preprints are preliminary reports that have not undergone peer review.
They should not be considered conclusive, used to inform clinical practice,
or referenced by the media as validated information.

Tide-Gauge Observations of Long-Period Harbour Oscillations Along the Venezuelan Caribbean Coast Following the 24 June 2026 Earthquake Doublet

Carlos José Araque-Pérez

carlos.araque@ugr.es

Universidad de Granada

José Bencomo-Fernández

Servicio de Hidrografía, Oceanografía y Navegación de la Armada de Venezuela

Ramón Ubina Carrero

Servicio de Hidrografía, Oceanografía y Navegación de la Armada de Venezuela

Marieglys Barrientos-Reyes

Servicio de Hidrografía, Oceanografía y Navegación de la Armada de Venezuela

Michael Schmitz

Central University of Venezuela

Research Article

Keywords: tide gauge, harbour oscillation, earthquake doublet, Venezuela, Caribbean Sea, time-frequency analysis

Posted Date: November 18th, 2026

DOI: https://doi.org/10.21203/rs.3.rs-11118151/v1

License: This work is licensed under a Creative Commons Attribution 4.0 International License.
Read Full License

Additional Declarations: No competing interests reported.

Tide-Gauge Observations of Long-Period Harbour Oscillations Along the Venezuelan Caribbean Coast Following the 24 June 2026 Earthquake Doublet

C. Araque-Pérez[1], J. Bencomo-Fernández[2], R. Ubina[2], M. Barrientos-Reyes[2], M. Schmitz[3]

[1] Andalusian Institute of Geophysics and Prevention of Seismic Disasters, University of Granada, Granada, Spain.
[2] Hydrography, Oceanography and Navigation Service, Venezuelan Navy, Catia La Mar, Venezuela.
[3] Department of Geophysics, Faculty of Engineering, Central University of Venezuela, Caracas, Venezuela

Abstract

Identifying tsunami signals from near-field tide gauges is challenging when an earthquake occurs close to the coast and the instruments are installed inside harbour basins. We analyse previously unavailable sea-level records from La Guaira, Puerto Cabello and Pampatar following the 24 June 2026 northern Venezuela earthquake doublet. La Guaira and Puerto Cabello were sampled at six-minute intervals; Pampatar was sampled at one-minute intervals and resampled to a common six-minute grid. Astronomical tides were estimated independently using robust harmonic analysis, and non-tidal residuals were examined in the time, spectral and time-frequency domains. La Guaira recorded the strongest response, with a first four-hour trough-to-crest residual range of 1.174 m, a post-event RMS 4.24 times the pre-event value, and spectral enhancement concentrated mainly between 18 and 30 min. The initial excursions coincided with anomalous within-record depth variability, and thus their hydrodynamic and instrumental contributions cannot be separated unequivocally. Puerto Cabello recorded a smaller range of 0.176 m and an RMS ratio of 1.33, with enhanced oscillations centred around 43-47 min and extending into longer periods. Pampatar showed no robust stationary spectral increase and an RMS ratio of 0.77. Comparison with published finite-fault virtual-gauge traces suggests broad amplitude-scale consistency at La Guaira, whereas the stronger observed contrast with Puerto Cabello remains unresolved; no corresponding virtual gauge was available for Pampatar. Pairwise correlations were weak and period dependent. The records indicate a heterogeneous, site-specific, earthquake-associated harbour response rather than a demonstrably coherent tsunami at all three ports. They provide direct observational constraints for future tsunami modelling.

Keywords: tide gauge; harbour oscillation; earthquake doublet; Venezuela; Caribbean Sea; time-frequency analysis.

1. Introduction

Tsunamis produced primarily by strike-slip earthquakes are typically rarer than those linked to significant subduction-zone ruptures, as horizontal fault movement results in relatively minimal direct vertical deformation of the seafloor. Nonetheless, measurable and, in some cases, destructive tsunamis have been recorded subsequent to strike-slip earthquakes, especially when the rupture occurs near coastlines, engages with steep submarine slopes, encompasses secondary dip-slip deformation, or triggers underwater and coastal mass movements (Elbanna et al., 2021; Estrada et al., 2021; Hornbach et al., 2010; Tanioka & Satake, 1996). In these circumstances, lateral seafloor movement can substantially influence vertical water-column distortion, even if the earthquake's focal mechanism is primarily strike-slip (Tanioka & Satake, 1996).

The southern Caribbean plate boundary is characterised by distributed dextral deformation associated with the eastward motion of the Caribbean plate relative to South America. In Venezuela, a substantial component of this motion is accommodated by the Boconó-San Sebastián-El Pilar fault system, although deformation occurs across a comparatively broad

plate-boundary zone (Audemard, 1997; Audemard et al., 2007; Pérez et al., 2001; Pousse-Beltran et al., 2017). Several historical earthquakes occurring along this boundary have been associated with anomalous sea-level behaviour and reported tsunamis along the Venezuelan coast, demonstrating that the regional tsunami hazard is not restricted to conventional subduction-zone sources (Audemard & Guzman, 2017; Oropeza & Audemard, 2016).

On 24 June 2026, northern Venezuela was affected by two large earthquakes occurring less than one minute apart. Available seismic source solutions indicate predominantly dextral strike-slip faulting on steeply dipping structures, accompanied by a comparatively minor vertical component (USGS, 2026a, 2026b). The earthquake sequence was followed by anomalous sea-level behaviour along the Venezuelan coastline and by small-amplitude signals recorded at several regional monitoring stations across the Caribbean (Cazenave et al., 2026). The regional tectonic setting, preferred earthquake epicentres and focal mechanisms, and locations of the three Venezuelan tide gauges analysed in this study are shown in Figure 1.

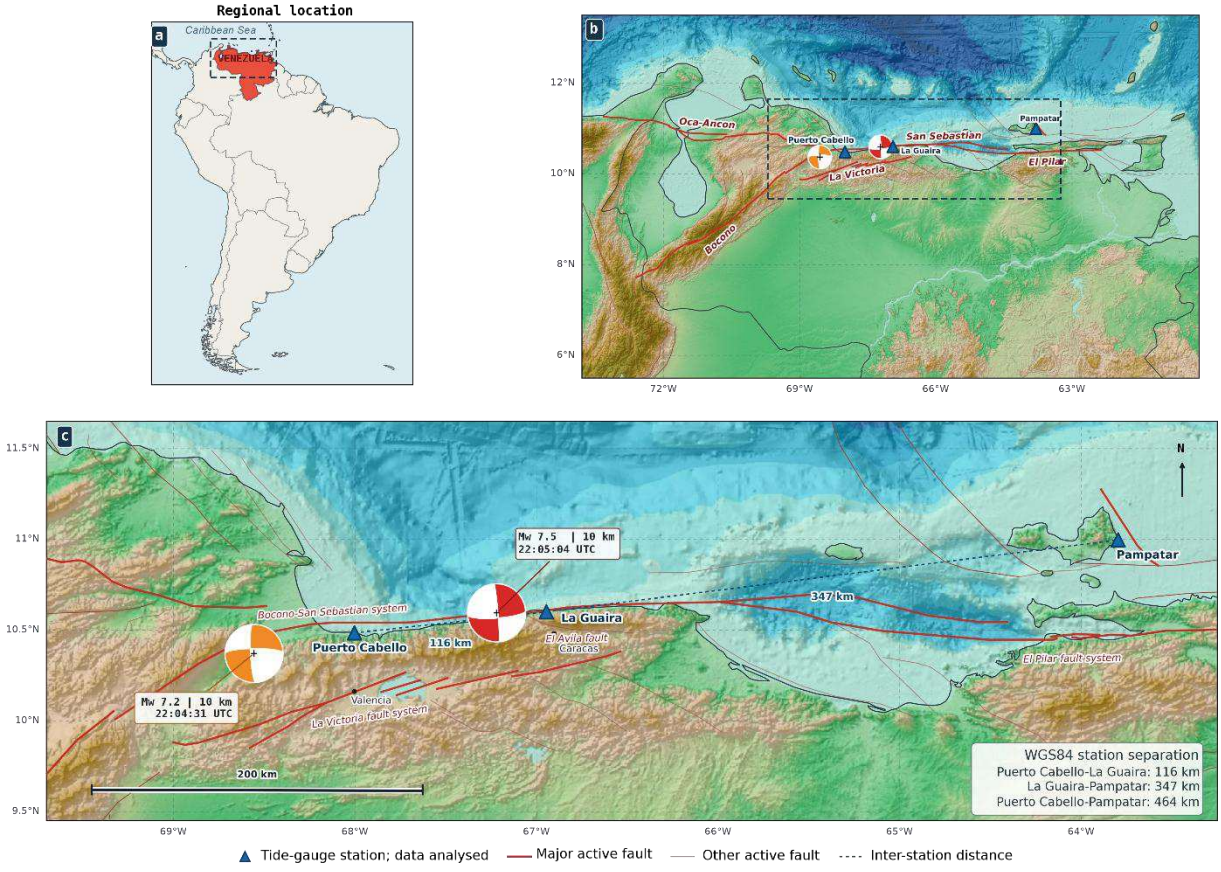


Figure 1. Geographic and tectonic setting of the 24 June 2026 northern Venezuela earthquake doublet and the tide-gauge network analysed in this study. (a) Location of Venezuela within northern South America and the Caribbean region. (b) Regional topographic and bathymetric relief mapped active faults, preferred USGS[1] earthquake epicentres and W-phase focal mechanisms, and locations of the Puerto Cabello, La Guaira and Pampatar tide gauges. The dashed rectangle indicates the area enlarged in the panel below. (c) Detailed view of the earthquake source region and the three-station tide-gauge network. Blue dashed segments connect adjacent stations, while the inset reports the WGS84 geodesic separations for all station pairs. The orange and red focal mechanisms correspond to the Mw 7.2 and Mw 7.5 earthquakes, respectively. Active-fault traces were extracted

[1] United States Geological Survey (USGS; https://www.usgs.gov/)

from the South American Risk Assessment Active Fault Database (Alvarado et al., 2019), as distributed through the GEM Global Active Faults Database (Styron & Pagani, 2020). Topographic and bathymetric relief was derived from the GEBCO2026 Grid (GEBCO, 2026).

Cazenave et al. (2026) modelled the resulting tsunami using uniform-slip and finite-fault source scenarios. Their results indicated that heterogeneous finite-fault models reproduced the arrival times and amplitudes observed at several regional Caribbean stations more successfully than simplified uniform-slip sources. The numerical simulations also predicted locally significant sea-level disturbances along the Venezuelan coast, including at virtual gauges located near La Guaira and Puerto Cabello. However, because no instrumental records from Venezuela were available to those authors, the predicted near-field amplitudes and waveforms could not be validated directly.

Near-field tide-gauge records are strongly influenced by local bathymetry, coastline configuration and the geometry of bays and harbours. Incoming tsunami energy can excite the natural oscillation modes of a semi-enclosed basin, modifying the amplitude, dominant period, phase and duration of the observed signal (Aránguiz et al., 2019; Bellotti et al., 2012; Rabinovich, 1997, 2009; Wang et al., 2021). Consequently, nearby tide gauges exposed to the same regional disturbance may record substantially different waveforms. This site-dependent response must be considered when comparing observations with virtual gauges extracted from regional numerical models.

This study presents previously unavailable sea-level records acquired by tide gauges installed within the ports of La Guaira, Puerto Cabello and Pampatar. Records for La Guaira and Puerto Cabello were acquired at six-minute intervals, whereas the Pampatar record was originally acquired at one-minute intervals and subsequently low-pass filtered and resampled onto a common six-minute grid for cross-station analysis. The stations are distributed along the northern Venezuelan margin, from Puerto Cabello and La Guaira on the mainland coast to Pampatar on Margarita Island, and differ in their distances from the earthquake source, coastal settings and harbour configurations. These observations provide direct constraints on the near-field sea-level response and allow the previously unvalidated numerical predictions reported by Cazenave et al. (2026) to be examined.

The objectives of this study are to (1) characterise the sea-level disturbances recorded at La Guaira, Puerto Cabello and Pampatar following the earthquake sequence; (2) separate the astronomical tide from the higher-frequency non-tidal residual; (3) identify event-related changes in spectral and time-frequency content relative to the pre-event background; (4) examine, as a secondary analysis, period-dependent waveform similarities and pairwise lagged relationships among the three stations; and (5) assess the consistency between the observed near-field response and the numerical predictions reported (Cazenave et al., 2026). Attention is given to distinguishing potentially propagating long-wave oscillations from harbour resonance, background sea-level variability and possible earthquake-induced instrumental disturbances.

2. Tectonic and coastal setting

2.1. Regional tectonic framework

Northern Venezuela lies within the broad and tectonically complex boundary zone between the Caribbean and South American plates (Figure 1). Geodetic observations indicate that the Caribbean plate moves approximately eastwards relative to stable South America at a rate of about 20 mm yr^{-1} (Pérez et al., 2001; Weber et al., 2001). This relative motion is not accommodated by a single discrete plate-boundary fault. Instead, deformation is distributed across a several-hundred-kilometre-wide zone characterised by dextral strike-slip faulting, transpression, crustal block rotation and locally significant shortening. (Erlich & Barrett, 1990; Pérez et al., 2001)

In Venezuela, the principal active structures form the Boconó–San Sebastián–El Pilar fault system. The Boconó Fault extends through the Venezuelan Andes and connects northwards with the San Sebastián Fault system along the north-central coast, whereas the El Pilar Fault accommodates much of the deformation in northeastern Venezuela. Additional structures, including the Oca–Ancón and La Victoria fault systems and several offshore fault strands, contribute to regional strain partitioning (Audemard, 2005; Audemard et al., 2000, 2006; Higgins et al., 2021; Pousse-Beltran et al., 2017). Geodetic and interferometric observations show that the relative plate motion is partitioned among several structures and that the degree of interseismic locking varies considerably along strike (Higgins et al., 2021; Reinoza et al., 2015).

This distributed deformation produces a segmented plate boundary in which individual earthquakes may involve mapped onshore faults, offshore continuations or previously unresolved structures. Consequently, the proximity of an epicentre to a mapped fault trace does not by itself demonstrate that the fault accommodated the complete rupture. The 24 June 2026 earthquake sequence occurred within the north-central part of this fault network, close to the Venezuelan coastline and near the transition between the Boconó and San Sebastián fault domains (Figure 1b, c). No definitive association of either earthquake with a single mapped surface trace is assumed in the present study.

2.2. The 24 June 2026 earthquake doublet

On 24 June 2026, two major earthquakes occurred in northern Venezuela within less than one minute. According to the current preferred USGS catalogue origins, the first event (E1; Mw 7.2) occurred at 22:04:31.806 UTC and was located 20 km east of San Felipe, at 10.3713° N, 68.5564° W. The second event (E2; Mw 7.5) occurred at 22:05:04.053 UTC and was located 20 km west of Catia La Mar, at 10.5955° N, 67.2205° W. The USGS assigns a hypocentral depth of 10 km to both earthquakes. The preferred origin times are separated by 32.247 s, and the epicentres are approximately 148 km apart (USGS, 2026a, 2026b).

The USGS W-phase moment-tensor solutions indicate predominantly strike-slip faulting on steeply dipping planes, with minor normal-slip components. Considering the approximately east–west-striking nodal plane in each solution, the strike, dip and rake are 269.7°, 74.4° and -168.9°, respectively, for E1, and 85.9°, 73.7° and -175.6° for E2 (USGS,

2026a, 2026b). Because each focal-mechanism solution defines two geometrically possible nodal planes, these parameters characterise one possible fault-plane orientation but do not, by themselves, identify the plane on which rupture occurred. The preferred USGS catalogue epicentres and the corresponding W-phase focal mechanisms used in this study are shown in Figures 1b and 1c.

The term 'earthquake doublet' is used here descriptively to refer to the close temporal association and comparable magnitudes of the two events; it does not imply that they were dynamically independent or that they ruptured separate fault structures. Source inversions and geodetic observations would be required to resolve the detailed relationship between the two ruptures.

The current preferred USGS catalogue origins differ from the source parameters adopted by Cazenave et al. (2026) for their uniform-slip tsunami scenarios. Those authors considered events of Mw 7.17 and Mw 7.48 at 22:04:33 and 22:05:11 UTC, respectively, and assigned source depths of 23.5 and 11.5 km. They applied a 39-s delay between the two earthquakes in the combined uniform-slip scenario. These adopted depths correspond to the centroid depths reported in the USGS W-phase moment-tensor products (USGS, 2026a, 2026b) and should not be interpreted as the current preferred catalogue hypocentral depths, which are 10 km for both events. This distinction must be considered when comparing the Venezuelan tide-gauge observations with the modelled arrival times and waveforms. Comparisons with the numerical predictions (Cazenave et al., 2026) therefore retain the temporal reference and source parameters employed in each simulation, whereas the epicentral distances and station relationships reported in the present study are calculated from the current preferred USGS catalogue epicentres.

2.3. La Guaira, Puerto Cabello, and Pampatar Harbours

The tide-gauge network examined in this study consists of three stations distributed along the northern Venezuelan margin (Figures 1b, c). La Guaira and Puerto Cabello are mainland ports located along the north-central coast, whereas Pampatar is situated on southeastern Margarita Island. The approximately east–west distribution of the stations provides observations at progressively different positions relative to the two earthquake epicentres and across contrasting mainland and insular coastal settings. Figure 2 displays the positions of the tide gauges within their respective harbour basins, along with photographs of the instruments' installations.

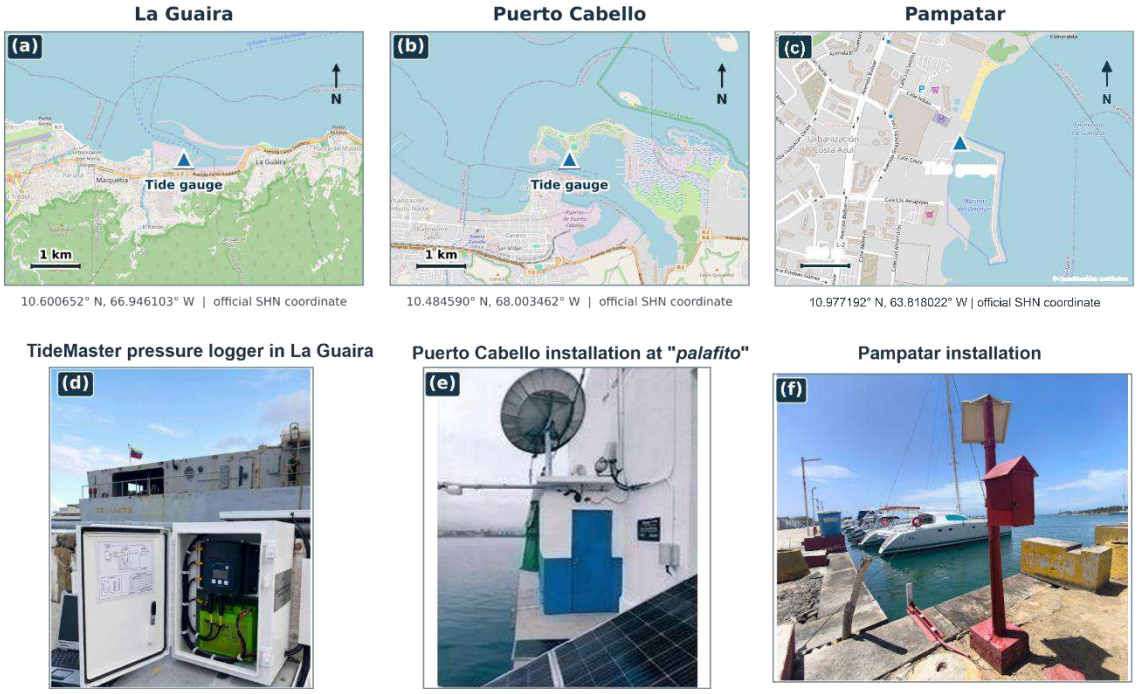


Figure 2. Local setting of the Venezuelan tide-gauge stations. (a–c) Harbour-scale maps of La Guaira, Puerto Cabello and Pampatar, respectively, showing the tide-gauge locations, harbour entrances and principal basin configurations. (d–f) Photographs of the corresponding tide-gauge installations. The coordinates of the stations were obtained from the 2026 technical station sheets provided by the Venezuelan Hydrographic Service (SHN). All coordinates are referenced to the WGS84 geodetic system.

The La Guaira tide gauge is installed within the Port of La Guaira at 10.600652° N, 66.946103° W. Based on the current USGS epicentres, the station lies approximately 30 km from E2 and 178 km from E1. Its location close to the eastern earthquake makes it the nearest instrumental sea-level record considered in this study. The Puerto Cabello station is installed at the “Palafito” site within the Puerto Cabello Naval Base, at 10.484590° N, 68.003462° W. It lies between the two epicentral locations, approximately 62 km from E1 and 87 km from E2. The tide-gauge position and coordinate reference are taken from the 2026 technical station sheet provided by the Venezuelan Hydrographic Service (SHN; see station sheet in Supplementary Material). The Pampatar tide gauge is located within Pampatar Harbour on Margarita Island. It is located at 10.97719° N, 63.81802° W. This position is approximately 377 km from E2 and 525 km from E1.

The geodesic distances between Puerto Cabello and La Guaira, La Guaira and Pampatar, and Puerto Cabello and Pampatar are approximately 116, 347, and 464 km, respectively. All coordinates and distances reported here refer to the WGS84 reference system. The source-to-station values represent epicentral distances and should not be interpreted as minimum distances to the finite rupture surface.

Because all three instruments are installed inside harbour basins, their records represent the combined effects of the incoming long-wave disturbance and the local hydrodynamic response of each port. Harbour entrance geometry, basin dimensions, water depth, coastal orientation and internal reflection can alter the amplitude, phase, dominant period and duration of the recorded oscillations (Monserrat et al., 2006). The three records are therefore

treated as site-specific sea-level responses rather than direct measurements of the offshore tsunami waveform. Instrument characteristics, temporal sampling and sea-level processing procedures are described separately in Section 3.

3. Tide-gauge data

Sea-level records from La Guaira, Puerto Cabello and Pampatar were provided by the SHN. The dataset consists of pressure-derived water-depth measurements acquired by tide gauges installed inside the three harbour basins. Because the geographical positions and coastal settings of the stations are described in Section 2.3 and shown in Figures 1 and 2, this section focuses on the instrumental metadata, temporal coverage, sampling characteristics and quality-control procedures applied to the records.

3.1. Instruments and station metadata

All three stations were equipped with Valeport TideMaster digital pressure tide gauges. The instruments installed at La Guaira, Puerto Cabello and Pampatar have serial numbers 89616, 89617 and 89615, respectively. The TideMaster export files contain timestamp, pressure-derived depth, within-record depth standard deviation (*Depth stdev*), battery and instrument-status fields, together with several ancillary meteorological fields. Only the timestamp, depth, depth standard deviation and status fields were used in this study because the meteorological fields contained no usable measurements.

Depth was reported in metres relative to the local instrumental reference. No transformation to a common vertical datum was applied because the analyses focus on temporal sea-level variations and non-tidal residuals at each station rather than on differences in absolute water level among the three ports. The *Depth stdev* field was retained as an independent diagnostic of short-term instrumental variability and was not used to correct or smooth the recorded sea level.

The coordinates and technical characteristics of the stations are summarised in Table 1. The positions of the La Guaira and Puerto Cabello instruments were obtained from the SHN station sheets (Supplementary Material) and are referenced to WGS84.

Table 1. Instrumental metadata and sampling characteristics of the three tide-gauge stations. Coordinates are referenced to WGS84.

Station	Coordinates	Instrument	Header Mode	Native sampling interval	Calibration metadata
La Guaira	10.600652° N, 66.946103° W	TideMaster S/N 89616	B2	6 min	February, 2024
Puerto Cabello	10.484590° N, 68.003462° W	TideMaster S/N 89617	B2	6 min	February, 2024
Pampatar	10.977191° N, -63.81802° W	TideMaster S/N 89615	B1	1 min	March, 2026

3.2. Data coverage, time reference, and sampling

Although the supplied files extend beyond the period immediately surrounding the earthquake sequence, the three records were restricted to a common analysis interval extending from 12:00 on 16 June to 12:00 on 30 June 2026. This 14-day interval provides the same pre-event baseline and post-event observation period for all stations. On the common six-minute grid, including both endpoints, each station series contains 3361 possible time steps.

The La Guaira record was acquired natively at six-minute intervals and is complete throughout the common analysis interval, providing 3361 observations. Puerto Cabello was also sampled natively every six minutes and contains 3359 observations. Two consecutive measurements are absent from this record at 15:30 and 15:36 on 22 June 2026. These missing values occur more than two days before the earthquake sequence and therefore do not affect the immediate event window.

Pampatar was originally sampled at one-minute intervals. Within the common interval, 20107 of the 20161 expected one-minute measurements were available. The 54 missing observations occur in four short gaps: 16:14–16:32 on 16 June, 10:24–10:34 on 19 June, 13:05–13:19 on 22 June, and 15:21–15:29 on 24 June. None of these gaps overlap the earthquake origin times.

For consistent inter-station comparisons, the Pampatar record was low-pass filtered and resampled from its native one-minute sampling interval onto the same six-minute grid used at La Guaira and Puerto Cabello. Short internal gaps were first filled by linear interpolation on the native one-minute grid to permit continuous filtering. An anti-alias polyphase finite-impulse-response filter with a Kaiser window was then applied before decimation by a factor of six. Of the resulting 3361 six-minute intervals, 3349 were derived entirely from directly observed one-minute measurements, whereas 12 contained at least one interpolated native value and were retained with a corresponding quality flag. Resampling was performed solely to establish a homogeneous dataset for comparison among stations; the original one-minute Pampatar observations were preserved.

The technical sheets specify Venezuelan Standard Time (VET; UTC−4) as the station time reference for the three stations. The USGS earthquake origin times were converted from UTC to VET before comparison with the tide-gauge records. All dates and times shown in the time-series and time-frequency figures are therefore expressed in VET. At the common six-minute sampling interval, the corresponding Nyquist period is 12 minutes; spectral energy approaching this lower-period limit must consequently be interpreted with caution.

3.3. Quality control and record harmonisation

The original TideMaster text exports were parsed independently for each station. Non-data header rows, blank fields and control characters introduced by the export format were discarded. Records were then arranged chronologically and examined for malformed timestamps, non-numeric depth values, sampling irregularities, gaps, repeated timestamps and instrument-status codes.

Several of the supplied files were repeated exports of the same measurement intervals. These files were verified to be byte-identical and were removed before the station records were merged. No conflicting depth measurements were found among the duplicated exports. All retained raw measurements carried an instrument-status value of zero, and no observations were rejected based on the status field.

The original observations were not subjected to automatic despiking, amplitude clipping or manual removal, particularly during the period immediately following the earthquake doublet. This was important at La Guaira, where the largest short-duration variation coincides closely with the earthquake sequence and must be evaluated as a potential combination of hydrodynamic response and earthquake-induced instrumental disturbance. The associated *Depth stdev* values were therefore retained and examined alongside the pressure-derived depth series.

Linear interpolation was used only when a continuous, regularly sampled sequence was required for digital filtering, spectral estimation or time-frequency analysis. Interpolated intervals remained explicitly flagged and were excluded from statistics intended to describe directly observed measurements. Robust exclusion of anomalous values was applied only during estimation of the astronomical tidal component, as described in Section 4.1, to prevent transient disturbances from biasing the harmonic fit; these values were not deleted from the observed sea-level series.

Following quality control and temporal harmonisation, the three datasets were maintained on an identical six-minute grid covering 16–30 June 2026. All subsequent station-specific figures and inter-station comparisons were calculated using this common temporal framework, while preserving information on the native sampling interval and observational status of each measurement.

4. Methods

All numerical processing was conducted in Python using NumPy (Harris et al., 2020) and SciPy routines (Virtanen et al., 2020). Unless otherwise stated, the three station records were analysed on the common six-minute grid extending from 12:00 VET on 16 June to 12:00 VET on 30 June 2026. The same processing parameters were applied to La Guaira, Puerto Cabello and Pampatar.

4.1. Astronomical tide estimation and removal

The astronomical tide was estimated independently at each station using classical harmonic analysis (Pawlowicz et al., 2002). The tidal model was fitted to the longest continuous record available from each instrument rather than only to the 14-day common interval. This approach increased the temporal basis available for separating the principal tidal constituents while preserving the common interval for subsequent inter-station comparisons. The recorded water level *h(t)* was presented as:

$$h(t) = a_0 + a_1(t - t_c) + \sum_{k=1}^{K}[A_k \cos(\omega_k t) + B_k \sin(\omega_k t)] + \varepsilon(t) \qquad (1)$$

where a_0 is the mean water level, a_1 is a linear trend, t_c is the temporal midpoint of the fitted record, ω_k is the known angular frequency of constituent (k), A_k and B_k are station-specific coefficients estimated by least squares, and $\varepsilon(t)$ represents the component of the observed record that is not explained by the harmonic model.

In Equation (1), $K=5$ and the index k represent the *M2*, *S2*, *N2*, *K1* and *O1* astronomical tidal constituents. These constituents were selected because their frequency separations could be resolved over the shortest station record used in the analysis. Closely spaced constituents requiring substantially longer records were not fitted independently. The periods of *M2*, *S2*, *N2*, *K1* and *O1* are 12.4206, 12.0000, 12.6583, 23.9345 and 25.8193 h, respectively (Rusdin et al., 2024). Their angular frequencies are defined in Equation (2), where P_k is the period of constituent k.

$$\omega_k = \frac{2\pi}{P_k} \qquad \textbf{(2)}$$

Measurements between 12:00 VET on 24 June and 06:00 VET on 25 June were excluded from the estimation of the tidal coefficients to prevent the earthquake-associated disturbance from influencing the predicted astronomical tide. The initial least-squares solution was followed by an iterative robust fitting procedure. At each iteration, the preliminary residual median and its scaled median absolute deviation were calculated as $1.4826\,\mathrm{median}|\varepsilon_i - \mathrm{median}(\varepsilon)|$ (Leys et al., 2013).

Observations differing from the residual median by more than five times the residual variability (σ_{MAD}) were excluded from the following iteration. The procedure was repeated until the retained set remained unchanged or a maximum of five iterations was reached. These observations were excluded only from the estimation of the tidal coefficients and were not removed from the measured water-level series.

The predicted tidal component $T(t)$ was evaluated at every timestamp of the common grid. The non-tidal sea-level residual was then calculated as:

$$R(t) = h(t) - T(t) \qquad \textbf{(3)}$$

All subsequent time-domain, spectral and time-frequency analyses were performed on $R(t)$. The residuals were analysed independently for each station, and no adjustment was applied to force their mean levels or amplitudes to agree.

4.2. Time-domain characterisation

The origin time of the first earthquake, 22:04:31.806 UTC on 24 June 2026, corresponding to 18:04:31.806 VET, was adopted as the common event reference time (t_0). The second earthquake occurred at 18:05:04.053 VET, only 32.247 s after the first. Because this separation is substantially shorter than the common six-minute sampling interval, the individual contributions of the two earthquakes cannot be resolved in the tide-gauge records. The doublet was therefore treated as a temporally unresolved forcing interval for the observational analysis, without implying that the two earthquakes constituted a single

physical source. The first common-grid measurement following both earthquakes corresponds to 18:06 VET.

The event-centred time series presented for each station extends from 12:00 VET on 24 June to 06:00 VET on 25 June. Quantitative post-event metrics were calculated over the four-hour interval 18:06 ≤ t < 22:06 VET, beginning with the first common-grid measurement following the doublet. For each station, the maximum and minimum residuals and their respective occurrence times were identified within this interval. The trough-to-crest residual amplitude was calculated as:

$$A_{\mathrm{TC}} = R_{\max} - R_{\min} \qquad \textbf{(4)}$$

where R_{max} and R_{min} are the maximum and minimum non-tidal residuals, respectively. The root-mean-square residual for a time window (w) was calculated as:

$$R_{\mathrm{RMS,w}} = \sqrt{\frac{1}{Nw}\sum_{i=1}^{Nw} R_i^2} \qquad \textbf{(5)}$$

where R_i is the residual sea level at observation i, and Nw is the number of valid observations within the corresponding time window. Both A_{TC} and $R_{\mathrm{RMS,w}}$ are expressed in metres.

A four-hour pre-event interval, 14:00 ≤ t < 18:00 VET on 24 June, was used to calculate the reference pre-event RMS. The relative increase in sea-level variability following the earthquake was expressed using the dimensionless Q_{RMS} ratio.

$$Q_{\mathrm{RMS}} = \frac{R_{\mathrm{RMS,post}}}{R_{\mathrm{RMS,pre}}} \qquad \textbf{(6)}$$

where $R_{\mathrm{RMS,post}}$ and $R_{\mathrm{RMS,pre}}$ represent the RMS values calculated over the four-hour post-event and pre-event intervals, respectively. This ratio allows the event-related increase in variability to be compared among stations without comparing their absolute instrumental water levels. Values of Q_{RMS}>1 indicate that residual sea-level variability increased following the earthquake doublet.

Background variability was characterised over the common pre-event interval extending from 12:00 VET on 16 June to 12:00 VET on 24 June. A robust estimate of background residual variability ($\sigma_{\mathrm{MAD,bg}}$) was calculated as:

$$\sigma_{\mathrm{MAD,bg}} = 1.4826 \times \mathrm{median}_{i\in\mathcal{B}}\left(\left|R_i - \mathrm{median}_{j\in\mathcal{B}}\left(R_j\right)\right|\right) \qquad \textbf{(7)}$$

where B denotes the background interval, R_i the residual value in the observation I, and $\mathrm{median}_{j\in B}(\mathrm{R}_j)$ represents the median of all the residuals within the background interval. The factor 1.4826 makes the scaled median absolute deviation comparable to the standard deviation for normally distributed data (Leys et al., 2013). Because $R(t)$ is expressed in metres, $\sigma_{\mathrm{MAD,bg}}$ is also expressed in metres.

The maximum *Depth stdev* value recorded during the first 12 minutes following t_0 was retained as an instrumental diagnostic. At the common six-minute sampling interval, this calculation included the measurements at 18:06 and 18:12 VET. The *Depth stdev* variable was evaluated separately from the non-tidal residual and was not incorporated into the trough-to-crest amplitude, RMS, or RMS-ratio calculations. Its purpose was to help assess whether the initial sea-level excursions were accompanied by an unusual increase in within-record measurement variability.

4.3. Spectral and time-frequency analysis

Spectral changes associated with the earthquake sequence were evaluated by comparing two six-hour intervals of equal duration. The background interval extended from 12:00 to 18:00 VET on 24 June, whereas the post-event interval extended from 18:06 VET on 24 June to 00:06 VET on 25 June. Each interval therefore contained 60 measurements on the common six-minute grid.

Power spectral densities were estimated using the Thomson multitaper method (Araque-Pérez, 2024; Thomson, 1982). Each six-hour residual segment was demeaned and linearly detrended before spectral estimation. Four discrete prolate spheroidal sequence tapers were generated using a time-bandwidth product of 2.5. The individual tapered spectra were subsequently combined using their spectral-concentration eigenvalues as weights. The resulting power spectral densities were expressed in square metres times minutes (m^2 min), because frequency was represented in cycles per minute.

Post-event and background spectra were calculated using identical parameters. The post-event-to-background spectral power ratio was calculated as:

$$G(P) = \frac{S_{\mathrm{post}}(P)}{S_{\mathrm{background}}(P)} \qquad \textbf{(8)}$$

where P is the period in minutes, $S_{\mathrm{post}}(P)$ is the post-event power spectral density at period P, and $S_{\mathrm{background}}(P)$ is the corresponding background power spectral density. Because the numerator and denominator have identical units, $G(P)$ is dimensionless. Values of $G(P)>1$ indicate increased post-event spectral power, whereas $G(P)<1$ indicates lower power relative to the background interval. This ratio was used to identify period ranges in which spectral energy increased following the earthquake, but it was not interpreted as a direct hydrodynamic amplification factor.

The temporal evolution of spectral power was examined between 00:00 VET on 23 June and 00:00 VET on 27 June. Two complementary time-frequency methods were applied. First, a short-time Fourier transform (STFT) was calculated using a 60-sample Hann window, equivalent to 360 min, with 54 samples of overlap. The resulting 90% overlap produced a 36-min displacement between consecutive time windows. Each segment was linearly detrended before transformation. A 512-point discrete Fourier transform was used to obtain a finely sampled frequency axis. The associated zero padding improved the graphical sampling of the spectrum but did not increase the intrinsic spectral resolution imposed by the six-hour window.

Second, a continuous wavelet transform was calculated using a complex Morlet mother wavelet with nondimensional frequency $\omega_0=6$, following Torrence and Compo (1998). Wavelet power was defined as the squared modulus of the complex wavelet coefficient. One hundred logarithmically spaced periods between 12 and 360 min were evaluated. The cone of influence was determined from the Morlet-wavelet e-folding time, and spectral features located within regions affected by edge effects were not used to identify the dominant periods.

Time-averaged STFT and wavelet spectra were calculated using time bins whose centres fell within the same six-hour background and post-event intervals employed in the multitaper analysis. A period range was considered a robust candidate event-related spectral band when the post-event power exceeded the corresponding background power, and the enhancement was independently supported by the multitaper spectrum and at least one of the two time-frequency representations. Isolated spectral maxima without corresponding temporal localisation were not interpreted as evidence of an event-related disturbance.

The common 6-minute sampling interval corresponds to a Nyquist period of 12 min (Cornélissen, 2014). Consequently, periods shorter than 12 min cannot be resolved. The 12–18 min range was retained in the figures to show the lowest formally resolvable portion of the spectrum, but it was marked as sampling-limited and excluded from quantitative interpretation. Periods between 180 and 360 min were displayed in the time-frequency diagrams to provide long-period context, but their interpretation was also limited by the finite six-hour analysis window. Quantitative comparisons of dominant periods therefore focused on the 18–180 min range.

4.4. Band-limited cross-correlation

Pairwise correlations were calculated as a secondary analysis to investigate whether the stations contained similar long-period waveforms. These calculations were not used as the principal evidence for identifying the earthquake-associated response.

The complete residual series from each station was first linearly detrended and filtered between periods of 18 and 180 min. A fourth-order Butterworth band-pass filter was applied in the forward and reverse directions to produce zero-phase filtering. Filtering was performed before extraction of the event window so that the beginning and end of the 12 h comparison interval were not affected by filter-starting transients.

The first 12 h following the earthquake doublet were extracted from the filtered records. Pearson correlation coefficients were then calculated as a function of lag for La Guaira–Puerto Cabello, La Guaira–Pampatar and Puerto Cabello–Pampatar. The procedure was applied to the complete 18–180 min band and repeated for the 18–30, 30–60 and 60–180 min sub-bands to assess the period dependence of waveform similarity.

The lag search was restricted to ±180 min. This limit ensured that at least 75% of the original 12 h window remained in every correlation calculation and prevented poorly constrained maxima from being selected at significant lags. A positive lag indicates that the

second station in a pair follows the first. Both the zero-lag correlation and the maximum correlation within the permitted lag interval were retained.

Because band-pass filtering and harbour resonance introduce strong serial dependence, the correlation coefficients were treated descriptively and were not interpreted using significance tests that assume independent observations. In particular, the lag producing the maximum correlation was not interpreted directly as a tsunami travel time. Similar oscillation periods can produce apparently favourable correlations even when the corresponding wave trains have different origins, arrival times or harbour responses (Dean & Dunsmuir, 2015).

4.5. Arrival-time and travel-time assessment

Candidate disturbance onsets were determined independently at each station rather than inferred from the pairwise correlation maxima. For this purpose, the detided residuals were compared with the pre-event background distribution. The background median and σ_{MAD} were calculated over the 12 h preceding t_0, excluding the final 30 min to reduce possible contamination associated with the beginning of the event-processing window.

A candidate onset was identified as the first post-event grid time for which the absolute departure from the background median exceeded three times σ_{MAD} in at least two of three consecutive measurements. The candidate was then compared with the time evolution of wavelet power integrated over the 18–180 min band. An onset was retained as a sustained long-period disturbance only when it was followed by an increase in band-integrated wavelet power lasting for at least 30 min.

The *Depth stdev* series was examined at the same time. A sudden residual excursion accompanied by an isolated increase in *Depth stdev*, but without a sustained increase in long-period wavelet power, was classified as instrumentally ambiguous rather than assigned unequivocally to a propagating water-level disturbance. Where the threshold and time-frequency criteria were not satisfied, no objective arrival time was assigned.

The apparent delay at the station (i) was expressed as

$$\Delta t_i = t_{a,i} - t_0 \qquad \textbf{(9)}$$

where $t_{a,i}$ is the candidate onset time. Because the records were compared at 6-min intervals, the temporal resolution of the resulting onset estimates cannot be better than 6 min. Additional uncertainty arises from the gradual emergence of low-amplitude oscillations and the finite temporal width of the spectral and wavelet windows.

For a descriptive comparison, the La Guaira and Puerto Cabello virtual-gauge traces for FFM Delouis and FFM USGS were extracted from Cazenave et al. (2026). The labelled UTC and amplitude axes were used to place the traces beside the observed residuals on common scales. The original panels provide approximately four minutes per horizontal pixel; no unique numerical model time series was reconstructed. Columns affected by overlap with the earthquake-origin marker were excluded. Observations retain their six-minute sampling, and no fitted time shifts or amplitude normalisation were applied. The comparison concerns the

visible amplitude scale and broad temporal evolution, rather than model RMS, spectra, arrival times or waveform correlations.

Geodesic source-to-station and inter-station distances were used only to describe the spatial configuration of the network. This study did not calculate the propagation velocity by dividing these distances by the correlation lags or observed onset delays because tsunami travel paths are controlled by spatially variable bathymetry and need not coincide with the direct geodesic connection between two locations. Moreover, the measured signals include the local response of each harbour and cannot be treated as unmodified offshore waveforms.

5. Results

5.1. La Guaira record

The La Guaira record was complete throughout the 14-day common analysis interval. Following removal of the astronomical tide, the pre-event residual had a scaled background median absolute deviation of 0.033 m. The earthquake doublet was followed immediately by a sequence of large, rapidly alternating residual excursions (Figure 3). The first post-event measurement, at 18:06 VET, had a residual of +0.127 m. This was followed by residuals of −0.463 m at 18:12, +0.547 m at 18:18 and −0.627 m at 18:24 VET.

Within the first four hours, the maximum and minimum residuals were therefore +0.547 and −0.627 m, respectively, giving a trough-to-crest range of 1.174 m. The post-event RMS was 0.201 m, compared with 0.047 m during the preceding four-hour interval, resulting in an RMS ratio of 4.24 (Table 2). The maximum *Depth stdev* during the first 12 min was 0.161 m, compared with a pre-event median value of 0.013 m. This pronounced increase in within-record variability coincided with the beginning of the large residual excursions.

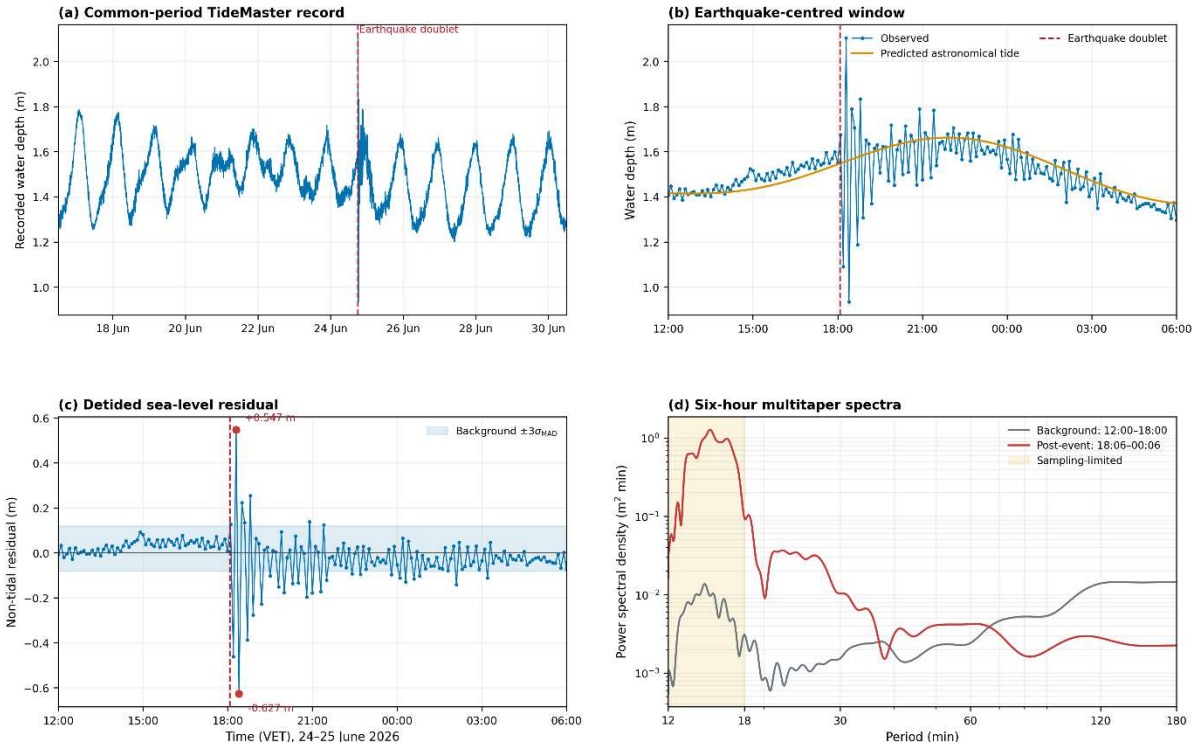


Figure 3. Sea-level observations at La Guaira harbour. (a) Complete record for the common analysis interval. (b) Observed water depth and predicted astronomical tide during the earthquake-centred window. (c) Non-tidal residual, with labelled extrema for the first four post-event hours. (d) Background and post-event multitaper spectra. The dashed line marks the first earthquake, and the shaded 12–18 min band indicates the sampling-limited range. Times are given in VET (UTC−4).

The six-hour post-event multitaper spectrum showed its largest power near a period of 18 min, immediately above the sampling-limited interval (Figure 3d). Integrated spectral power increased by factors of 26.0 and 2.33 in the 18–30 and 30–60 min bands, respectively. In contrast, power in the 60–180 min band decreased to 0.33 of the corresponding background value. The STFT and Morlet wavelet results also showed a temporally localised enhancement beginning close to the earthquake's origin time and concentrated predominantly between 18 and 30 min (Figure 4). The post-event-to-background wavelet-power ratio was 16.4 in this band and 2.15 between 30 and 60 min.

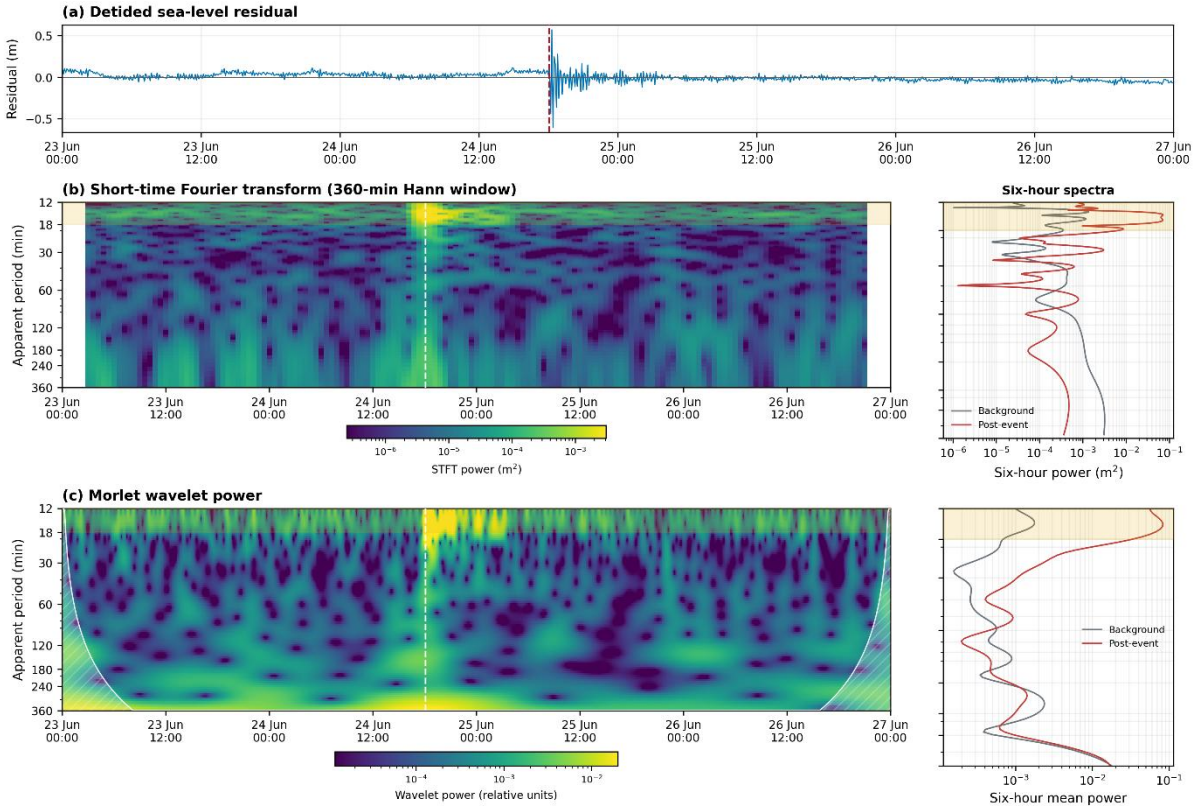


Figure 4. Time–frequency analysis of the La Guaira non-tidal residual. (a) Residual sea level. (b) Short-time Fourier transform power and corresponding six-hour background and post-event spectra. (c) Morlet wavelet power and corresponding mean spectra. The dashed line marks the first earthquake, hatched areas indicate the cone of influence, and the shaded 12-18 min band is sampling-limited.

5.2. Puerto Cabello record

The Puerto Cabello residuals showed substantially smaller post-event excursions than those observed at La Guaira (Figure 5). During the first four hours, the minimum residual was −0.076 m at 18:54 VET, whereas the maximum was +0.100 m at 21:42 VET. The resulting trough-to-crest range was 0.176 m. The post-event RMS was 0.048 m, compared

with a pre-event value of 0.036 m, giving an RMS ratio of 1.33. The scaled background median absolute deviation was 0.039 m.

The maximum *Depth stdev* during the first 12 min was 0.041 m and occurred at 18:06 VET. Although substantially smaller in absolute terms than the corresponding La Guaira value, it was higher than the Puerto Cabello pre-event median of 0.009 m.

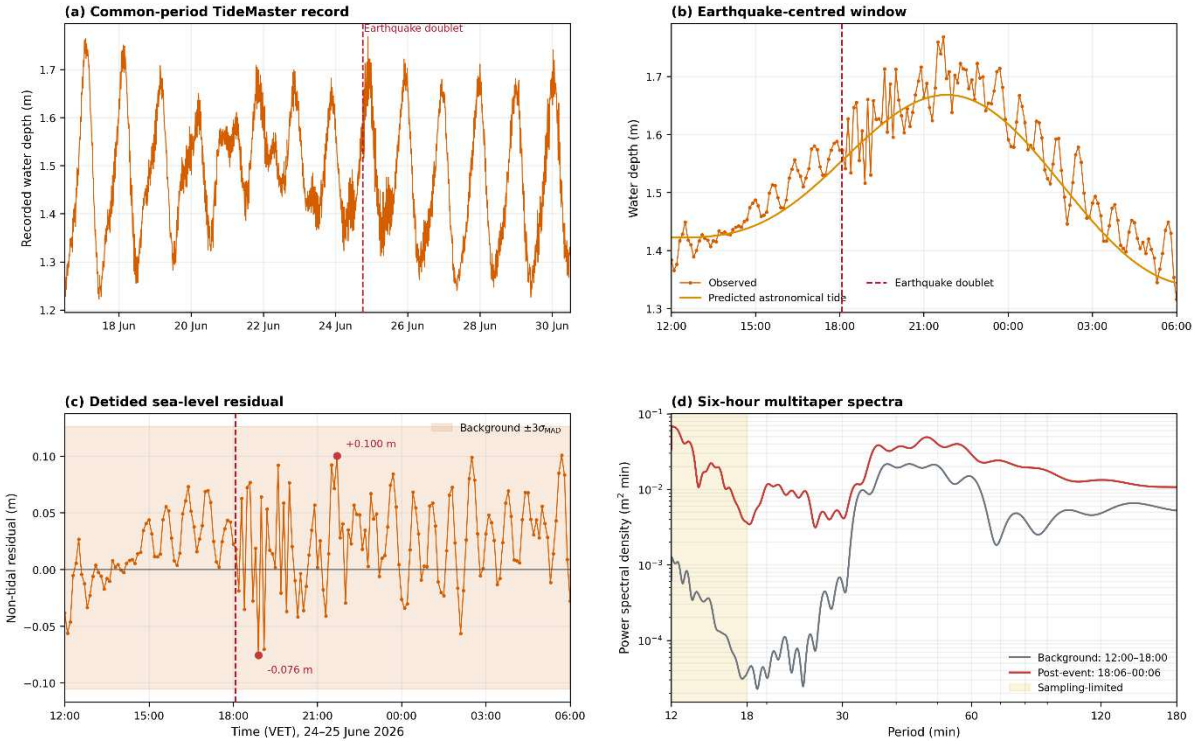


Figure 5. Sea-level observations at Puerto Cabello. (a) Complete record for the common analysis interval. (b) Observed water depth and predicted astronomical tide during the earthquake-centred window. (c) Non-tidal residual, with labelled extrema for the first four post-event hours. (d) Background and post-event multitaper spectra. The dashed line marks the first earthquake, and the shaded 12–18 min band indicates the sampling-limited range. Times are given in VET (UTC−4).

The post-event spectrum was dominated by a broader band centred at approximately 43-47 min (Figures 5d and 6). Multitaper spectral power increased relative to the background in all three analysed period bands. The corresponding ratios were 55.5 for 18-30 min, 2.11 for 30-60 min and 3.39 for 60–180 min. The particularly large ratio in the shortest band reflected the very low pre-event power within that interval and did not correspond to the maximum absolute spectral power, which occurred within the 30–60 min band.

The STFT and wavelet diagrams showed that oscillations around 40–50 min were already present before the earthquake but increased in power and temporal continuity afterwards. Additional post-event enhancement occurred between 60 and 180 min. Consequently, the Puerto Cabello response contained both short-period variability and a more persistent intermediate- to long-period component.

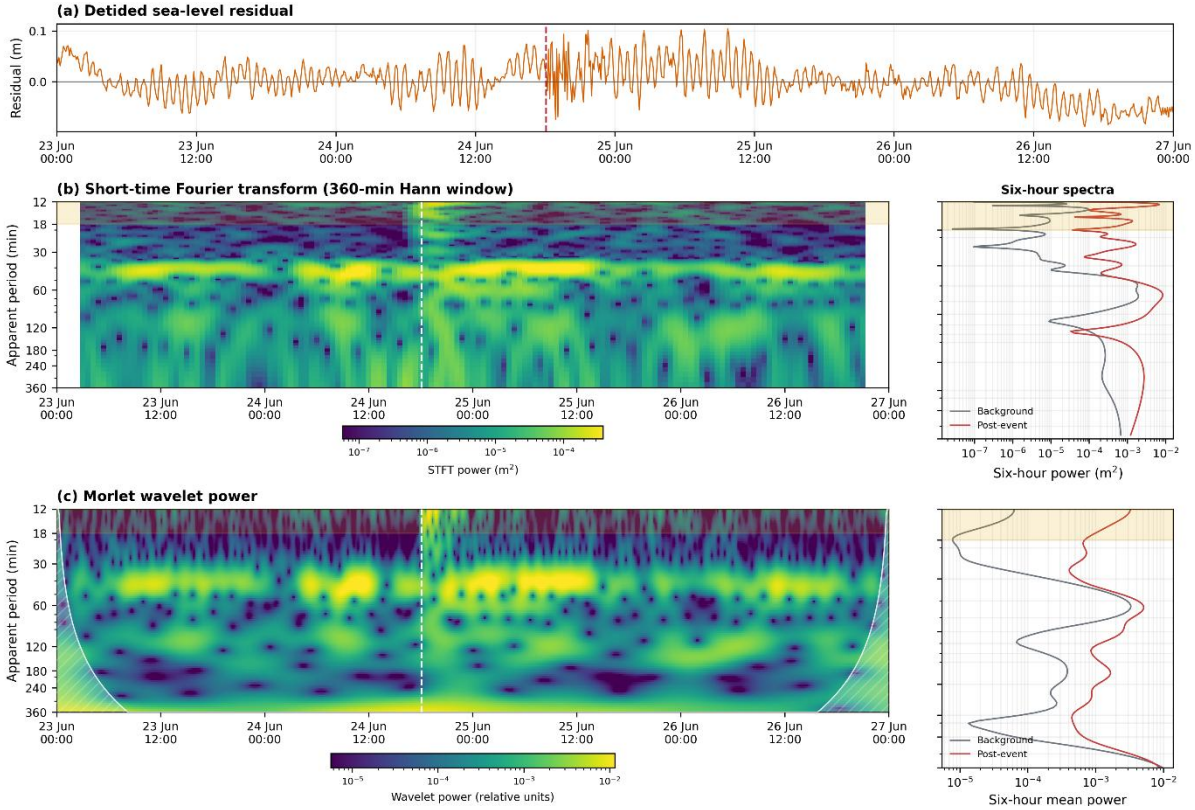


Figure 6. Time–frequency analysis of the Puerto Cabello non-tidal residual. (a) Residual sea level. (b) Short-time Fourier transform power and corresponding six-hour background and post-event spectra. (c) Morlet wavelet power and corresponding mean spectra. The dashed line marks the first earthquake, hatched areas indicate the cone of influence, and the shaded 12–18 min band is sampling-limited.

5.3. Pampatar record

The Pampatar residuals had amplitudes comparable to the pre-event variability throughout much of the event-centred window (Figure 7). The minimum residual during the first four hours was −0.061 m at 18:48 VET, and the maximum was +0.055 m at 21:36 VET, producing a trough-to-crest range of 0.116 m. The post-event RMS was 0.029 m, lower than the pre-event value of 0.037 m, and the resulting RMS ratio was 0.77. The scaled background median absolute deviation was 0.039 m.

The maximum resampled *Depth stdev* during the first 12 min was 0.047 m, compared with a background median of 0.036 m. Unlike at La Guaira and Puerto Cabello, this value did not constitute a pronounced departure from the preceding instrumental variability.

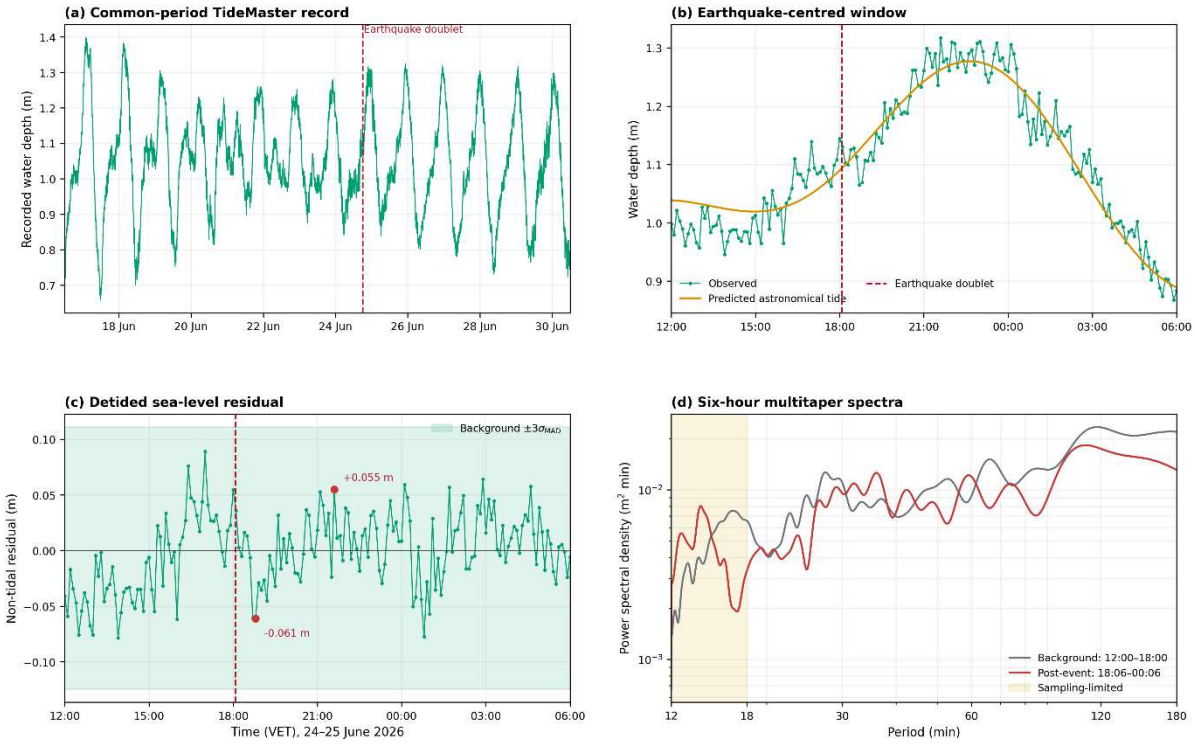


Figure 7. Sea-level observations at Pampatar. (a) Complete record for the common analysis interval. (b) Observed water depth and predicted astronomical tide during the earthquake-centred window. (c) Non-tidal residual, with labelled extrema for the first four post-event hours. (d) Background and post-event multitaper spectra. The native one-minute observations were anti-alias filtered before resampling to six minutes. The dashed line marks the first earthquake, and the shaded 12–18 min band is sampling-limited.

The largest post-event multitaper power occurred at approximately 111 min. However, the power during this period was only 0.82 of its background value. Integrated multitaper power ratios were 0.76, 1.06 and 0.75 for the 18–30, 30–60 and 60–180 min bands, respectively. The total post-event power between 18 and 180 min was 0.85 of the background value.

The STFT and wavelet representations showed a broad increase within the 60–180 min range, with post-event-to-background ratios of 1.47 and 1.82, respectively (Figure 8). Nevertheless, the strongest wavelet power occurred close to the upper limit of the quantitatively interpreted period range, and comparable long-period variability was present before the earthquake. Because this enhancement was not independently supported by the stationary multitaper spectrum, it did not satisfy the predefined criterion for a robust event-related spectral band.

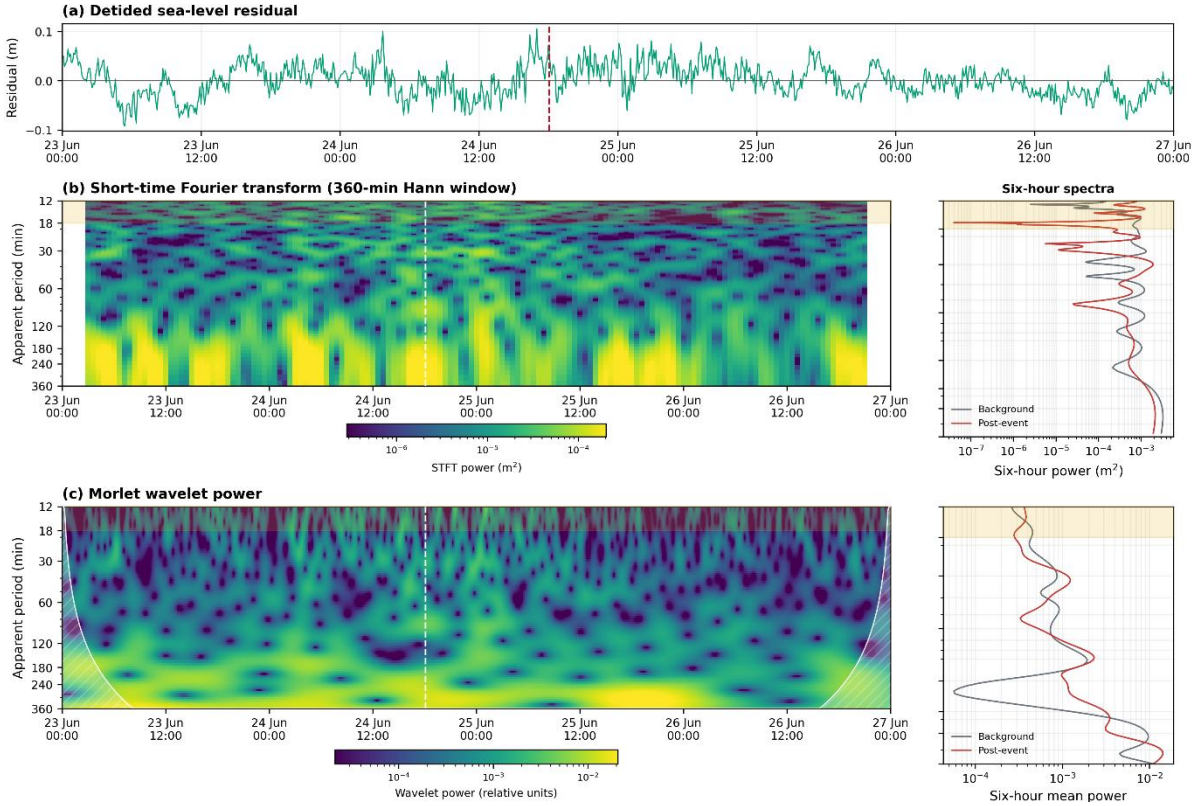


Figure 8. Time–frequency analysis of the Pampatar non-tidal residual after anti-alias filtering and resampling to the common six-minute grid. (a) Residual sea level. (b) Short-time Fourier transform power and corresponding six-hour background and post-event spectra. (c) Morlet wavelet power and corresponding mean spectra. The dashed line marks the first earthquake, hatched areas indicate the cone of influence, and the shaded 12–18 min band is sampling-limited.

5.4. Inter-station comparison

The time-domain response differed markedly among the three stations (Figure 9 and Table 2). The La Guaira trough-to-crest range was approximately 6.7 times greater than the range recorded at Puerto Cabello and 10.1 times greater than that recorded at Pampatar. La Guaira's post-event RMS was approximately 4.1 and 7.0 times the corresponding Puerto Cabello and Pampatar values, respectively. By contrast, the background scaled median absolute deviations were similar, ranging from 0.033 to 0.039 m. The large inter-station differences in post-event amplitude therefore cannot be attributed solely to differences in background residual variability.

Table 2. Time-domain metrics calculated from the detided residuals. All amplitudes are expressed in metres and times in VET.

Station	Maximum residual	Minimum residual	Trough-to-crest	Pre-event RMS	Post-event RMS	Post-/pre-event RMS ratio
La Guaira	+0.547 at 18:18	-0.627 at 18:24	1.174	0.047	0.201	4.24
Puerto Cabello	+0.100 at 21:42	-0.076 at 18:54	0.176	0.036	0.048	1.33
Pampatar	+0.055 at 21:36	-0.061 at 18:48	0.116	0.037	0.029	0.77

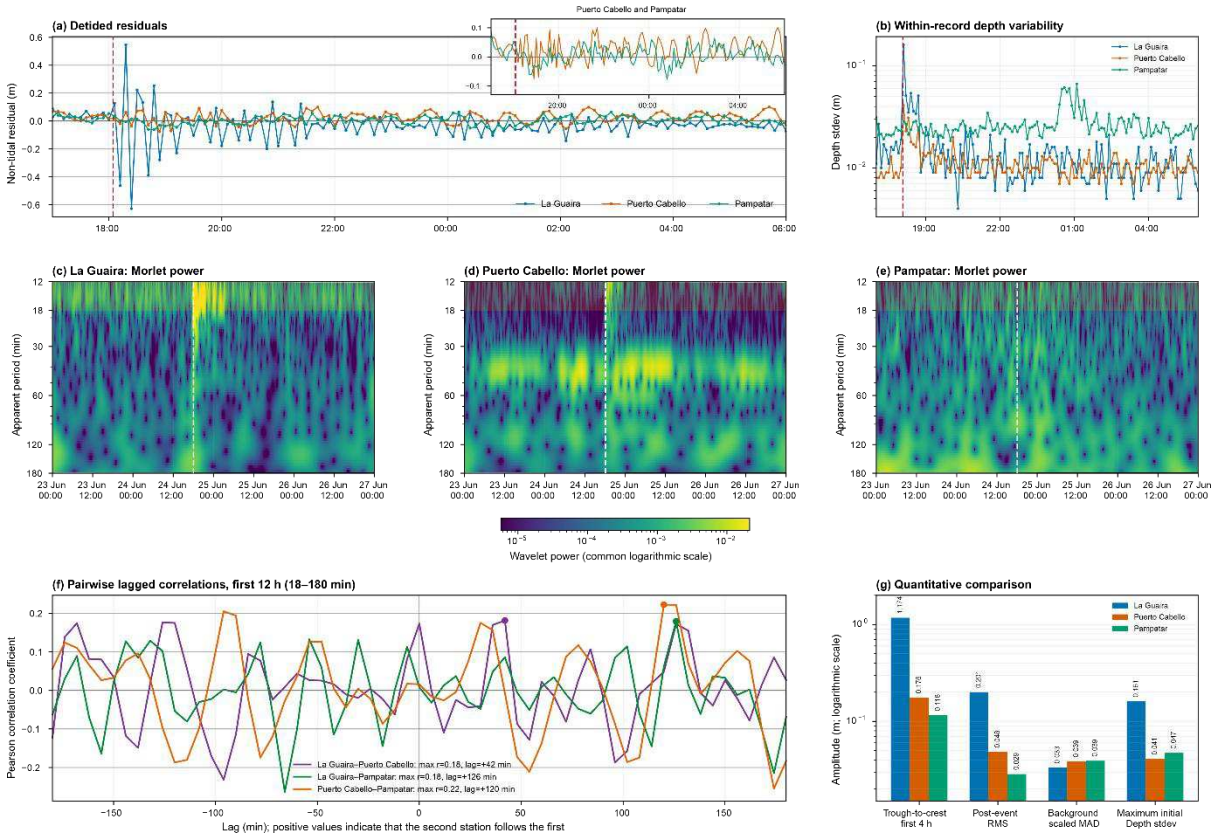


Figure 9. Comparison of the La Guaira, Puerto Cabello and Pampatar records. (a) Earthquake-centred non-tidal residuals; the inset enlarges the Puerto Cabello and Pampatar records. (b) Within-record water-depth variability. (c–e) Morlet wavelet power shown using a common logarithmic colour scale. (f) Pairwise lagged correlations of the 18–180 min band-limited residuals during the first 12 post-event hours. Positive lags indicate that the second station follows the first. (g) Comparison of trough-to-crest range, post-event RMS, background scaled MAD and maximum initial *Depth stdev*. Correlation lags are descriptive and are not interpreted as tsunami travel times.

Correlations calculated over the complete 18-180 min band were weak. The maximum correlation between La Guaira and Puerto Cabello was (r=0.18) at a lag of +42 min, whereas the La Guaira-Pampatar and Puerto Cabello-Pampatar maxima were (r=0.18) at +126 min and (r=0.22) at +120 min, respectively. Their zero-lag correlations were 0.17, 0.01 and 0.02.

Higher correlations were obtained in individual sub-bands, but the corresponding lags were not consistent. For La Guaira and Puerto Cabello, the maximum correlation was (r=0.55) at +60 min in the 18–30 min band but (r=0.50) at -144 min in the 60–180 min band. The strongest Puerto Cabello-Pampatar long-period correlation was (r=0.42) at +132 min. The changes in both magnitude and sign of the optimum lag across period bands demonstrate that no single lag produced a stable alignment of the station pairs.

5.5. Dominant periods and candidate onset times

The three records exhibited different dominant spectral characteristics. La Guaira was characterised by a short-period post-event enhancement concentrated mainly between 18- and 30-min. Puerto Cabello showed lower-amplitude oscillations with maximum absolute spectral power at approximately 43–47 min and additional energy extending into the 60–180 min band. Pampatar contained longer-period variability, but its post-event stationary spectral

power did not exceed the background sufficiently to satisfy the event-related classification criterion.

At La Guaira, the objective residual threshold was first exceeded at 18:06 VET, corresponding to 1.47 min after the first earthquake's origin. This candidate onset was accompanied by a sustained increase in 18–180 min wavelet power and was therefore retained by the predefined detection procedure. However, it also coincided with the largest *Depth stdev* value, requiring separate assessment of its hydrodynamic and instrumental contributions.

At Puerto Cabello and Pampatar, the residual threshold was not exceeded in at least two of three consecutive measurements. Consequently, no objective onset time was assigned at either station. The period-dependent cross-correlation lags were therefore not interpreted as inter-station propagation or tsunami travel times.

6. Discussion

6.1. Hydrodynamic signal versus instrumental disturbance

The observations provide clear evidence that the earthquake doublet was followed by an abrupt change in the La Guaira tide-gauge record. However, the earliest residual excursions cannot be interpreted unequivocally as the arrival of a freely propagating tsunami. The first available measurement after the doublet was recorded at 18:06 VET, approximately 1.47 min after E1 and only 56 s after E2. This measurement was followed by rapidly alternating positive and negative residuals and coincided with a pronounced increase in *Depth stdev*. Near-source pressure records may contain overlapping contributions from ground motion, transient pressure changes and hydrodynamic waves, making the seismic and tsunami components difficult to separate without high-rate measurements or an independent record of ground acceleration (Angeli et al., 2025; Kubota et al., 2021). The initial La Guaira measurements must therefore be regarded as instrumentally and hydrodynamically ambiguous.

Nevertheless, the complete La Guaira response cannot be explained solely as an isolated instrumental disturbance. The residual oscillations continued beyond the interval containing the maximum *Depth stdev*, and the post-event RMS was more than four times its pre-event value. In addition, the multitaper, STFT and wavelet analyses consistently showed an increase in power within the 18–30 min band beginning close to the earthquake origin time. This persistence and concentration of energy within a defined period range is more consistent with a hydrodynamic oscillation excited within or near the harbour than with a single pressure sensor spike. Harbour geometry and local bathymetry can selectively amplify and prolong frequency components of an incoming disturbance (Rabinovich, 1997, 2009). The 18-min spectral maximum, however, lies close to the sampling-limited range and corresponds to only approximately three measurements per oscillation. Its precise period and amplitude should consequently be interpreted with caution because coarse tide-gauge sampling can distort or alias tsunami waveforms (Leonard, 2006).

A secondary submarine mass movement triggered by the earthquake cannot be excluded for La Guaira. A predominantly strike-slip earthquake may destabilise weak sediments on the adjacent shelf or upper slope through strong ground shaking, cyclic shear and increased pore pressure, even when direct vertical seafloor displacement is limited. Similar earthquake-landslide mechanisms have been discussed for the 2010 Haiti and 2018 Palu earthquakes, while the 1998 Papua New Guinea tsunami provides a well-documented example of an earthquake-triggered submarine slump (Hornbach et al., 2010; Carvajal et al., 2019; Tappin et al., 2008). The present tide-gauge records do not demonstrate that such a failure occurred offshore La Guaira; this remains a testable hypothesis requiring bathymetric or geophysical evidence.

The value of 1.174 m measured at La Guaira should therefore be described as the trough-to-crest range of the harbour residual during the first four post-event hours, rather than as the height of an offshore tsunami wave. This distinction is essential because the recorded amplitude may incorporate the initial response to ground shaking, local harbour amplification and the subsequent oscillatory response. The observations support the occurrence of an earthquake-associated sea-level disturbance at La Guaira, but they do not permit the first recorded excursion to be attributed exclusively to tsunami propagation.

The evidence is less conclusive at Puerto Cabello. The initial increase in *Depth stdev* was smaller than at La Guaira, the post-event RMS increased by only a factor of 1.33, and the objective onset criterion was not satisfied. Oscillations with periods of approximately 40–50 min were present before the earthquake and became more energetic and temporally persistent afterwards. This behaviour is compatible with the earthquake-related enhancement of a pre-existing harbour mode, but it does not provide an unambiguous tsunami arrival time. At Pampatar, the post-event RMS was lower than its pre-event value, the initial *Depth stdev* remained comparable to the background variability, and the stationary spectrum did not identify a robust post-event increase. The Pampatar record therefore does not provide positive evidence of an earthquake-associated disturbance under the detection criteria adopted here. The analysis does not demonstrate the absence of a weak offshore wave; it merely suggests that any such signal could not be distinguished reliably from the local background at this station.

Taken together, the records support a tiered interpretation: La Guaira contains a clear earthquake-associated response with an initially ambiguous instrumental or co-seismic component followed by sustained harbour oscillations; Puerto Cabello contains a weaker possible enhancement of pre-existing harbour variability; and Pampatar shows no robust event-related change. This interpretation avoids assigning the entire recorded disturbance either to instrumental malfunction or to a propagating tsunami and provides the appropriate basis for the subsequent comparison of the contrasting harbour responses.

6.2. Contrasting harbour responses

The three stations did not record scaled versions of a single common waveform. La Guaira exhibited a trough-to-crest residual range of 1.174 m, compared with 0.176 m at Puerto Cabello, and 0.116 m at Pampatar (Figure 9; Table 2). These differences were also evident in

the post-event RMS values and dominant spectral bands. By contrast, the background scaled median absolute deviations were similar at the three stations. The markedly different post-event responses therefore cannot be explained solely by differences in background variability or data processing.

In addition to the source-to-station distance, the position of each instrument within its harbour must also be considered. A tide gauge installed inside a port records the incoming long wave after it has interacted with the continental shelf, harbour entrance, breakwaters, internal basins and other coastal structures. These interactions can attenuate some frequency components while amplifying and prolonging others through reflection and resonance (Bellotti et al., 2012; Rabinovich, 1997, 2009). Observations following the 2003 Boumerdès-Zemmouri tsunami similarly showed that neighbouring harbours experienced markedly different effects depending on their geometry, entrance orientation and local response (Sahal et al., 2009). The three Venezuelan records should therefore be interpreted as measurements of distinct harbour responses rather than as direct observations of an unmodified offshore waveform.

The La Guaira instrument occupies a comparatively exposed position within a major coastal port and is located approximately 30 km from the E2 epicentre. Its greater proximity to the eastern earthquake and more direct hydraulic connection with the adjacent coastal waters provide plausible conditions for a stronger initial response. Nevertheless, source proximity alone cannot account quantitatively for the observed amplitude because source directivity, propagation path, local bathymetry and amplification within the port remain unresolved. The concentration of post-event energy in the 18–30-minute band suggests that the incoming disturbance excited a relatively short-period response within the La Guaira harbour system. Consequently, the large observed residual range represents a locally modified harbour signal and should not be interpreted directly as the amplitude of the offshore disturbance.

The Puerto Cabello tide gauge is installed at the "*Palafito*" site within the protected harbour of the Puerto Cabello Naval Base (Figure 2). This location is more sheltered than the La Guaira station and is separated from the open coast by the internal configuration of the port. Such sheltering provides a plausible explanation for the absence of residual excursions comparable to those recorded at La Guaira, because the most direct component of an incoming disturbance may be reduced before reaching the instrument. This interpretation remains qualitative, however, because no harbour-scale hydrodynamic model is presently available to calculate the attenuation between the harbour entrance and the tide-gauge site.

A protected location does not necessarily suppress all long-period motion. Semi-enclosed and interconnected harbour basins can selectively retain energy when the forcing overlaps with one of their natural oscillation modes (Gao et al., 2017). The Puerto Cabello spectrum was dominated by a broader band centred at approximately 43–47 min, and oscillations within this range were already present before the earthquake but became stronger and more persistent afterwards. This behaviour is consistent with a site-dependent harbour response involving frequency-dependent amplification, attenuation and resonance (Aránguiz et al.,

2019; Bellotti et al., 2012; Horrillo et al., 2008). The smaller amplitudes and longer periods observed at Puerto Cabello are therefore consistent with the local response of the protected harbour, but the contribution of sheltering cannot be isolated without a harbour-scale hydrodynamic model. These observations do not establish a longer tsunami travel time.

Pampatar differs from the other stations in both geographical position and coastal setting. The station is located approximately 377 km from E2 and 525 km from E1, on Margarita Island. Its greater source distance makes a lower-amplitude disturbance plausible because the wave field may have undergone geometrical spreading and complex transformation before reaching the eastern Venezuelan coast. Nevertheless, distance alone cannot predict the response of a coastal gauge. Propagation direction, intervening bathymetry, island effects, harbour orientation and coupling with local natural modes can all influence whether an offshore disturbance produces a detectable signal inside a particular basin. Moreover, harbour gauges located close to nodal areas of a natural oscillation mode may record relatively small amplitudes even when other parts of the same coastal system are affected (Bertin et al., 2018).

At Pampatar, the post-event RMS was lower than the pre-event value, the initial *Depth stdev* remained comparable with its background level, and the stationary spectrum did not show a robust event-related increase. The record therefore provides no positive detection under the criteria applied in this study. This result should not be interpreted as demonstrating that no long wave reached Margarita Island. Rather, any disturbance arriving at Pampatar was either too small to be distinguished from the local background, poorly coupled with the response of the harbour, or insufficiently resolved by the available observations.

The weak pairwise correlations and the variation in optimum lag among the analysed period bands are consistent with these contrasting source distances and harbour configurations. Local sheltering, resonance and frequency-dependent amplification alter the phase and waveform recorded at each instrument, thereby reducing the similarity between stations. The calculated correlation lags consequently do not define a coherent sequence of arrivals and cannot be converted into propagation times. Quantifying the individual contributions of source distance, coastal propagation and harbour response would require high-resolution numerical models that explicitly represent the bathymetry, harbour entrances and internal configurations of La Guaira, Puerto Cabello and Pampatar.

6.3. Comparison with existing tsunami simulations

Cazenave et al. (2026) simulated the tsunami generated by the earthquake sequence using five source configurations: separate uniform-slip representations of the two earthquakes (S1 and S2), a combined uniform-slip scenario (S1+S2), and two heterogeneous finite-fault models referred to as FFM Delouis[2] and FFM USGS[3]. Their regional comparison with Caribbean sea-level stations indicated that the finite-fault models, particularly FFM USGS,

[2] FFM Delouis, finite-fault model developed by Bertrand Delouis (Geoazur, Université Côte d'Azur; https://acesse.one/a4voecg)
[3] FFM USGS, finite-fault model provided by the United States Geological Survey (https://earthquake.usgs.gov/data/finitefault/)

reproduced the observed amplitudes and arrival times more successfully than the uniform-slip scenarios. However, Venezuelan instrumental records were unavailable to those authors. Figure 10 compares their published finite-fault virtual-gauge traces with the observed residuals at La Guaira and Puerto Cabello. The common axes allow a descriptive assessment of amplitude scale and temporal evolution; the rasterised model curves do not support sample-by-sample waveform validation.

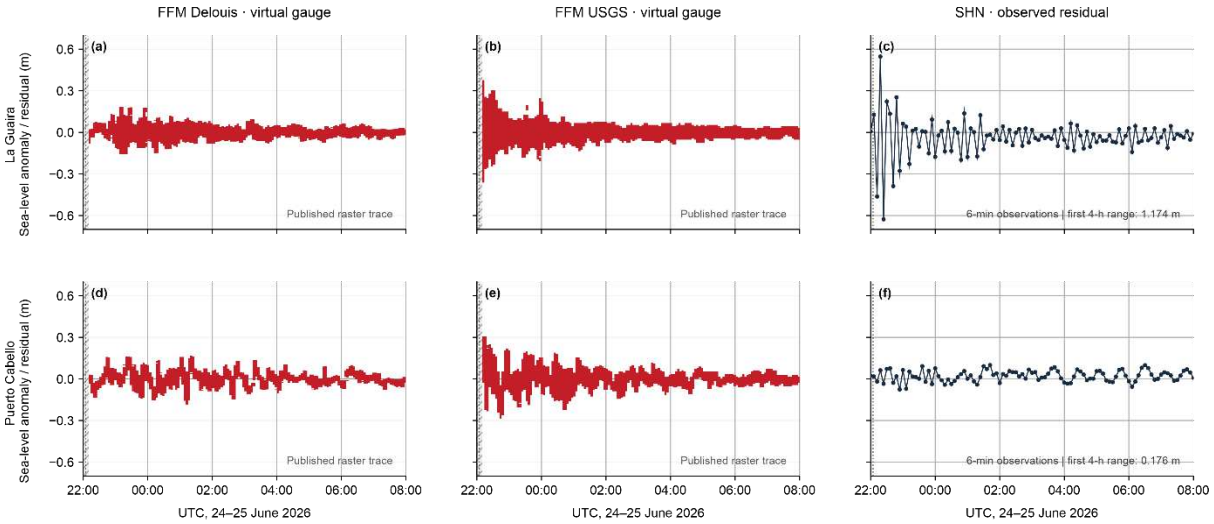


Figure 10. Published virtual-gauge predictions and observed non-tidal residuals at La Guaira (a–c) and Puerto Cabello (d–f). Model traces are adapted from the FFM Delouis (a, d) and FFM USGS (b, e) scenarios simulated by Cazenave et al. (2026); observations (c, f) retain six-minute sampling. All panels share the same time (UTC) and amplitude scales. Model traces retain their raster resolution; hatching marks origin-line overlap excluded from extraction. The dotted line marks E1.

At La Guaira, the observed residual shows a pronounced initial response followed by smaller oscillations (Figure 10c). FFM USGS also displays a strong early response followed by reduced visible amplitudes, whereas FFM Delouis shows a more gradual development of elevated oscillations (Figure 10a, b). During the first four post-event hours, the observed maximum absolute residual was 0.627 m, and the trough-to-crest range was 1.174 m. Cazenave et al. (2026) report an amplitude of approximately 0.50 m for the FFM USGS virtual gauge. These values indicate a broadly comparable order of magnitude, but the reported model amplitude is not a maximum independently measured over the observational four-hour window. It must also be distinguished from the observed trough-to-crest range.

This apparent agreement does not constitute a direct validation of the FFM USGS waveform. The earliest La Guaira measurements coincide with a pronounced increase in *Depth stdev* and may include contributions from ground shaking (Angeli et al., 2025) or transient instrumental response. Moreover, the observed signal was recorded inside the harbour and may have been amplified by local resonance (Roger et al., 2021). The six-minute sampling interval also prevents the detailed phase and waveform of the first oscillations from being reconstructed (Sahal et al., 2009). The observations therefore indicate consistency in order of magnitude, but they cannot determine how much of the recorded amplitude originated from offshore tsunami forcing and how much resulted from local harbour or instrumental effects.

The comparison at Puerto Cabello is less favourable. The maximum absolute residual was approximately 0.10 m, and the trough-to-crest range was 0.176 m (Figure 10f). The published finite-fault traces display larger visible excursions, especially for FFM USGS (Figure 10d, e); Cazenave et al. (2026) reports amplitudes of approximately 0.20 m for FFM Delouis and 0.40 m for FFM USGS. The observations thus show a stronger La Guaira–Puerto Cabello contrast than is apparent in these model traces. This is a descriptive discrepancy, rather than a measured model bias: the original simulated time series are unavailable for applying the observational sampling and identical amplitude statistics.

This difference is not necessarily evidence that the simulated offshore wave field was incorrect. The Puerto Cabello instrument is located within the protected naval-base harbour, where entrance geometry and internal basins may attenuate some components and amplify others. Such frequency-dependent harbour and shelf responses are documented by Rabinovich (2009) and Bellotti et al. (2012). In contrast, the approximately 460 m spatial resolution employed by Cazenave et al. (2026) cannot resolve individual harbour structures, restricted entrances, internal basins or the precise depth at the "*Palafito*" tide-gauge site. The authors themselves noted that the modelled depth of a virtual-gauge cell may differ substantially from the actual depth beside a pier or harbour structure. Consequently, the virtual gauge represents the coastal wave field at a regional-grid cell rather than the hydrodynamic response at the exact instrumental location.

The observed dominant periods also cannot be compared rigorously with the published simulations. Puerto Cabello exhibited oscillations around 43–47 min and additional long-period energy, whereas La Guaira exhibited its principal post-event enhancement between 18 and 30 min. These contrasting spectral responses are probably controlled partly by the natural modes of the two ports. Because the simulations did not resolve the internal harbour geometries, agreement in offshore or near-coastal amplitude would not necessarily produce agreement in period, phase or duration at the instruments. The published virtual-gauge waveforms should therefore not be expected to reproduce the complete tide-gauge records without higher-resolution harbour modelling.

No equivalent virtual gauge was included at Pampatar. The station lies outside the higher-resolution Venezuelan coastal grid used by Cazenave et al. (2026) and is represented only within their coarser regional domain. Their maximum-amplitude maps predicted tsunami propagation towards parts of the Venezuelan offshore-island region, especially in the finite-fault scenarios, but those maps do not provide a site-specific prediction for Pampatar harbour. The absence of a robust post-event increase in the Pampatar record consequently cannot be used to confirm or reject the simulations at that location.

Candidate arrival times provide only limited additional discrimination. The La Guaira threshold was exceeded at the first common-grid measurement after the doublet, but this onset is instrumentally ambiguous and has an uncertainty governed by the six-minute sampling interval. No objective onset was identified at Puerto Cabello or Pampatar. Therefore, the present observations cannot provide a reliable quantitative test of the simulated

travel times, and the cross-correlation lags should not be substituted for physical arrival times.

Overall, the Venezuelan tide-gauge records provide partial and spatially variable support for the simulations. The large La Guaira response is broadly consistent in scale with the stronger finite-fault prediction, particularly FFM USGS, whereas the smaller and longer-period Puerto Cabello response is not reproduced by the regional model. Pampatar lacks a directly corresponding virtual gauge and showed no robust event-related signal. The observations therefore confirm the importance of obtaining local instrumental constraints but do not uniquely favour one source model. A more rigorous validation would require rerunning the alternative source scenarios with nested harbour-scale bathymetric grids, extracting synthetic records at the precise instrument coordinates, sampling them at the observational interval and processing them using the same tidal-removal and spectral procedures applied to the measured records.

6.4. Implications for the Venezuelan monitoring network

The observations presented in this study have direct implications for tsunami monitoring along the Venezuelan Caribbean coast. Venezuela possesses historical seismic and sea-level records, together with institutions that operate the national seismic and tide-gauge networks (Acuña & Bosch, 2004; Palma et al., 2010). These provide complementary capabilities for earthquake-source characterisation and the detection of associated coastal sea-level disturbances. However, data from the two observational systems are not routinely integrated or made available through a common scientific framework, as demonstrated by the unavailability of the Venezuelan tide-gauge records for the regional analysis of Cazenave et al. (2026). Greater coordination and systematic data exchange between the institutions operating these networks would facilitate the detection, verification and scientific interpretation of locally generated sea-level disturbances.

FUNVISIS[4] was established in Venezuela approximately 54 years ago (Decree No. 1,053, República de Venezuela, 1972) and is currently attached to the Ministry for Science and Technology. The national legislation identifies the institution as a national technical and scientific reference for the prevention, monitoring, investigation, and management of seismic phenomena (Decree No. 5,420, República Bolivariana de Venezuela, 2026). In addition, the Intergovernmental Oceanographic Commission is part of the United Nations Educational, Scientific and Cultural Organization (IOC-UNESCO), where its Tsunami Programme currently designates FUNVISIS as the Venezuelan Tsunami Warning Focal Point within the Intergovernmental Coordination Group/Early Warning System for the Caribbean and Adjacent Regions (ICG/CARIBE-EWS), with the national civil protection authority serving as the alternate focal point (IOC-UNESCO, 2026a). Within this framework, a Tsunami Warning Focal Point acts as a continuously available national contact for receiving and disseminating tsunami information and contributes, in accordance with national procedures, to evaluating the threat to the country's coastline (IOC-UNESCO, 2014). FUNVISIS therefore plays a central role in the Venezuelan seismic and tsunami-warning chain,

[4] Venezuelan Foundation for Seismological Research (https://www.funvisis.gob.ve/).

especially in the areas of earthquake detection, rapid source characterisation, and technical interpretation.

The sea-level component is provided by SHN[5] of the Venezuelan Navy. Articles 185–193 of the Venezuelan Law on Marinas and Related Activities assign the SHN responsibility for conducting and coordinating hydrographic and related scientific activities, organising the collection and compilation of hydrographic, oceanographic and meteorological data, and producing official tide tables and other nautical information (Ley de Marinas y Actividades Conexas, 2014). The same legislation explicitly encourages coordination with international bodies and national organisations working in related fields. The SHN's national report to the International Hydrographic Organization also identifies oceanographic data management and tide-gauge instrumentation among its operational capabilities (SHN, 2024).

These complementary functions provide a sound basis for establishing a formal operational protocol between FUNVISIS and the SHN. Under such an arrangement, FUNVISIS could provide rapid earthquake parameters, source-mechanism information and preliminary assessments of tsunami potential, while the SHN could provide near-real-time sea-level measurements, station-status information and the metadata required for their interpretation. Such cooperation would not require either institution to relinquish responsibility for or custody of its observing systems. Instead, it would connect seismic detection with direct confirmation of the coastal response.

A joint protocol could define common data formats, time standards, quality-control procedures, event triggers and communication channels. It should also provide for the preservation of native-resolution observations, automated transmission of near-real-time sea-level data and the rapid exchange of station metadata, including sensor type, calibration history, vertical datum and documented interruptions. The present results indicate that six-minute records are sufficient to identify prominent long-period harbour oscillations, but they cannot resolve the individual response to earthquakes separated by only 32 s and may attenuate or alias shorter-period components. Retaining at least one-minute measurements, where technically feasible, would therefore improve both operational detection and subsequent scientific analysis.

The proposed coordination would also facilitate systematic comparison between observations and tsunami simulations, improve the distinction between hydrodynamic signals and earthquake-induced instrumental disturbances, and provide a national archive for future hazard assessments. Previous Venezuelan experience with CARIBE WAVE[6], the annual regional tsunami-warning exercise coordinated within the framework of ICG/CARIBE-EWS, has already emphasised the importance of coordinated participation by scientific institutions, civil protection authorities and coastal organisations (Aguilar Medina et al., 2011; IOC-UNESCO, 2026b). The 24 June 2026 earthquake sequence provides a practical demonstration of the value of this approach. Rather than indicating an absence of national capability, the

[5] Hydrography, Oceanography and Navigation Service, Venezuelan Navy (https://www.shn.mil.ve).
[6] https://www.tsunamizone.org/espanol/caribewave/

954 records analysed here show that substantial observational capacity already exists and could be
955 made more effective through formalised data exchange and sustained cooperation among
956 FUNVISIS, the SHN and the national civil protection system.

957 *6.5. Observational constraints and remaining uncertainties*

958 The results should be interpreted within the temporal resolution of the records and the
959 local harbour setting of the instruments. Each gauge measured the combined effects of the
960 incoming sea-level disturbance, harbour resonance, background variability and any short-
961 lived instrumental response to ground shaking. At La Guaira, the initial residual excursions
962 coincided with an increase in *Depth stdev*. The subsequent persistence and spectral
963 organisation of the oscillations support a hydrodynamic contribution, although the magnitude
964 of the initial instrumental component remains uncertain.

965 The six-minute sampling interval at La Guaira and Puerto Cabello sets a Nyquist period of
966 12 minutes and does not allow the responses to the two earthquakes to be resolved separately.
967 It also limits the precision with which the first sea-level arrival can be determined. Pampatar
968 was originally sampled at one-minute intervals but was filtered and resampled to six minutes
969 for inter-station comparison. In addition, the tidal model was restricted to five constituents
970 resolvable over the available records, and usable meteorological measurements were
971 unavailable. The residuals may therefore retain minor contributions from unresolved tidal or
972 environmental variability.

973 Because all three instruments are located within harbours, their records represent site-
974 specific coastal responses rather than unmodified offshore wave fields. The pairwise
975 correlations and their period-dependent lags are consequently treated as descriptive measures
976 and not as tsunami travel times. Similarly, comparison with Cazenave et al. (2026) evaluates
977 the consistency of the observations with the published simulations rather than providing a
978 complete model validation, because the virtual gauges and regional bathymetric grid do not
979 reproduce the precise instrument positions or internal harbour geometries. Future nested
980 modelling using detailed harbour bathymetry and the observed records would allow the
981 offshore wave contribution and local amplification to be quantified more precisely.

982 **7. Conclusions**

983 This investigation undertakes a comparative analysis of sea-level measurements at the
984 ports of La Guaira, Puerto Cabello, and Pampatar in the aftermath of the 24 June 2026
985 northern Venezuela earthquake doublet. Observational data from La Guaira and Puerto
986 Cabello were acquired at six-minute intervals, while the native one-minute time series from
987 Pampatar was filtered and resampled to align with the six-minute grid, thereby enabling
988 robust inter-station comparison. Following the independent removal of astronomical tides, the
989 records underwent time-domain, multitaper spectral, and time-frequency analyses.

990 La Guaira displayed the most pronounced response. In the initial four hours post-event, the
991 detided residual spanned a trough-to-crest range of 1.174 m, and the post-seismic RMS was
992 4.24 times greater than the pre-event figure. Spectral and time–frequency analyses revealed a

marked amplification, predominantly within the 18- to 30-minute band. Notably, the largest initial excursions coincided with a significant elevation in within-record depth standard deviation, precluding a definitive separation of hydrodynamic and instrumental contributions at this stage. Nevertheless, the persistence and spectral coherence of subsequent oscillations are indicative of a substantial harbour response directly associated with the earthquake.

Puerto Cabello exhibited a comparatively modest range of 0.176 m and an RMS ratio of 1.33. Oscillatory behaviour was dominated by periods centred near 43–47 minutes, with further spectral energy extending into the 60–180-minute band. This response is characteristic of a weaker, longer-period, and distinctly site-dependent signal within the protected confines of the naval-base harbour. Pampatar registered a range of 0.116 m and an RMS ratio of 0.77; its stationary spectrum showed no definitive post-event amplification, and thus the station did not meet the predefined positive detection criteria.

Pairwise correlations among the three stations were weak and strongly dependent on period band and lag. These lags cannot be interpreted as tsunami travel times because the records combine propagation effects, harbour resonance, local bathymetry, background variability and possible instrumental responses.

Comparison with published finite-fault virtual-gauge traces of Cazenave et al. (2026) indicates broadly comparable amplitude scales at La Guaira and a stronger observed contrast with Puerto Cabello than is apparent in the model figures. This descriptive comparison does not establish waveform agreement or uniquely favour a source model. Pampatar has no directly corresponding virtual gauge. The records provide local observational constraints for future quantitative evaluation using the original synthetic series and harbour-scale bathymetry.

Overall, the records indicate a heterogeneous and site-dependent earthquake-associated harbour response along the Venezuelan Caribbean coast, rather than a demonstrably coherent tsunami signal at all three ports. Preserving native-resolution observations, exchanging seismic and sea-level data between FUNVISIS and the SHN, and developing nested harbour-scale models would substantially improve future event interpretation and coastal monitoring.

Acknowledgements

The authors convey their gratitude to the University of Granada and the Andalusian Institute of Geophysics and Seismic Disaster Prevention for the committed time and institutional assistance necessary for data analysis and study development. Sincere thanks are extended to the Hydrography, Oceanography and Navigation Service of the Venezuelan Navy (SHN) for making the sea-level data available for scientific research. Additionally, the Central University of Venezuela (UCV) is acknowledged for its key contributions to the historical characterization of Venezuelan geology and tectonics.

Conflict of Interest

The authors declare no conflicts of interest relevant to this study.

Data availability

The complete dataset is available online at https://doi.org/10.6084/m9.figshare.33626185, following a six-month embargo period, facilitating further numerical modelling and hydrodynamic simulations in the Caribbean.

References

Acuña, G., & Bosch, W. (2004). Absolute comparison of satellite altimetry and tide gauge registrations in Venezuela. https://mediatum.ub.tum.de/1300515

Aguilar Medina, A., Romero, G., & Fra Rey, J. (2011). Implementación de un sistema de alerta temprana contra tsunami en la República Bolivariana de Venezuela: interacción institucional y desafíos planteados para el último eslabón de la cadena. VI Jornadas Venezolanas de Sismología Histórica, Caracas, Venezuela. . https://www.researchgate.net/publication/344725627_Implementacion_de_un_sistema_de_alerta_temprana_contra_tsunami_en_la_Republica_Bolivariana_de_Venezuela_Interaccion_institucional_y_desafios_planteados_para_el_ultimo_eslabon_de_la_cadena#fullTextFileContent

Alvarado, A., Audemard, F., Escobar, C. B., Boric, I. S., Perasso, J. C., Costa, C., Madera, G. F. D., García-Pelaez, J. A., Masquelin, E., Minaya, E., López, M. C., Paolini, M., Perez, I., SEGEMAR, G. de N. de, & Styron, R. (2019). the South American Risk Assessment Active Fault Database [Data set]. In Fondazione GEM. https://doi.org/10.13117/sara-active-faults

Angeli, C., Armigliato, A., Zanetti, M., Zaniboni, F., Romano, F., Bayraktar, H. B., & Lorito, S. (2025). Tsunami detection methods for ocean-bottom pressure gauges. Natural Hazards and Earth System Sciences, 25(3), 1169–1185. https://doi.org/10.5194/nhess-25-1169-2025

Aránguiz, R., Catalán, P. A., Cecioni, C., Bellotti, G., Henriquez, P. C., & González, J. (2019). Tsunami Resonance and Spatial Pattern of Natural Oscillation Modes with Multiple Resonators. Journal of Geophysical Research Oceans, 124(11), 7797–7816. https://doi.org/10.1029/2019jc015206

Araque-Pérez, C. J. (2024). Reevaluating soil amplification using multi-spectral HVSR technique in La Chana Neighborhood, Granada, Spain. Journal of Seismology, 28(4), 921–949. https://doi.org/10.1007/s10950-024-10227-2

Audemard, F. (1997). Holocene and historical earthquakes on the Boconó fault system, southern Venezuelan Andes: Trench confirmation. Journal of Geodynamics, 24, 155–167. https://doi.org/10.1016/s0264-3707(96)00037-3

Audemard, F. (2005). Paleoseismology in Venezuela: Objectives, methods, applications, limitations and perspectives. Tectonophysics, 408, 29–61. https://doi.org/10.1016/j.tecto.2005.05.034

Audemard, F., & Guzman, A. F. L. (2017). Reliability of first-hand accounts on the study of historical tsunamis in northeastern Venezuela (southeastern Caribbean Sea). Annals of Geophysics, 60(6). https://doi.org/10.4401/ag-7437

Audemard, F., Machette, M. N., Cox, J. W., Dart, R. L., & Haller, K. M. (2000). Map and database of Quaternary faults in Venezuela and its offshore regions [Report]. U.S. Geological Survey Open-File Report 00-18. https://doi.org/10.3133/ofr0018

Audemard, F., Singer, A., Soulas, J. P., & Mocquet, A. (2007). Quaternary faults and stress regime of Venezuela. In HAL (Le Centre pour la Communication Scientifique Directe). Centre National de la Recherche Scientifique. https://hal.science/hal-00154951

Bellotti, G., Briganti, R., & Beltrami, G. M. (2012). The combined role of bay and shelf modes in tsunami amplification along the coast. Journal of Geophysical Research Oceans, 117. https://doi.org/10.1029/2012jc008061

Bertin, X., Bakker, A. de, Dongeren, A. van, Coco, G., André, G., Ardhuin, F., Bonneton, P., Bouchette, F., Castelle, B., Crawford, W. C., Davidson, M., Deen, M., Dodet, G., Guérin, T., Inch, K., Leckler, F., McCall, R., Müller, H., Olabarrieta, M., … Tissier, M. (2018). Infragravity waves: From driving mechanisms to impacts. Earth-Science Reviews, 177, 774–799. https://doi.org/10.1016/j.earscirev.2018.01.002

Carvajal, M., Araya-Cornejo, C., Sepúlveda, I., Melnick, D., & Haase, J. S. (2019). Nearly instantaneous tsunamis following the Mw 7.5 2018 Palu earthquake. Geophysical Research Letters, 46, 5117–5126. https://doi.org/10.1029/2019GL082578

Cazenave, M., Roger, J., Philippon, M., Audemard, F., & Delouis, B. (2026). The tsunami triggered by the 24 June 2026 Venezuela earthquakes: tectonic context and tsunami modelling. In Research Square. https://doi.org/10.21203/rs.3.rs-10607566/v1

Cornélissen, G. (2014). Cosinor-based rhythmometry. Theoretical Biology and Medical Modelling, 11(1), 16. https://doi.org/10.1186/1742-4682-11-16

Dean, R. T., & Dunsmuir, W. T. M. (2015). Dangers and uses of cross-correlation in analyzing time series in perception, performance, movement, and neuroscience: The importance of constructing transfer function autoregressive models. Behavior Research Methods, 48(2), 783–802. https://doi.org/10.3758/s13428-015-0611-2

Decree No. 1,053, República de Venezuela, (1972). Creación de la Fundación Venezolana de Investigaciones Sismológicas (FUNVISIS) http://www.funvisis.gob.ve/nosotros.html

Decree No. 5,420, República BolIvariana de Venezuela, Gaceta Oficial de la República Bolivariana de Venezuela (2026). https://www.gacetaoficial.io/gaceta-oficial-43434-2026-08-11

Elbanna, A., Abdelmeguid, M., Ma, X., Amlani, F., Bhat, H. S., Synolakis, C. E., & Rosakis, A. J. (2021). Anatomy of strike-slip fault tsunami genesis. Proceedings of the National Academy of Sciences, 118(19). https://doi.org/10.1073/pnas.2025632118

Erlich, R. N., & Barrett, S. F. (1990). Cenozoic Plate tectonic history of the northern Venezuela-Trinidad Area. Tectonics, 9(1), 161–184. https://doi.org/10.1029/tc009i001p00161

Estrada, F., González-Vida, J. M., Peláez, J. A., Galindo-Zaldívar, J., Ortega, S., Macías, J., Vázquez, J. T., & Ercilla, G. (2021). Tsunami generation potential of a strike-slip fault tip in the westernmost Mediterranean. Scientific Reports, 11(1), 16253. https://doi.org/10.1038/s41598-021-95729-6

Gao, J., Ji, C., Gaidai, O., Liu, Y., & Ma, X. (2017). Numerical investigation of transient harbor oscillations induced by N-waves. Coastal Engineering, 125, 119–131. https://doi.org/10.1016/j.coastaleng.2017.03.004

GEBCO, B. C. G. (2026). The GEBCO_2026 Grid - a continuous terrain model for oceans and land at 15 arc-second intervals. [Data set]. In NERC Environmental Data Service. https://doi.org/10.5285/4f68d5c7-45eb-f999-e063-7086abc036fa

Harris, C. R., Millman, K. J., Walt, S. J. van der, Gommers, R., Virtanen, P., Cournapeau, D., Wieser, E., Taylor, J., Berg, S., Smith, N. J., Kern, R., Picus, M., Hoyer, S., Kerkwijk, M. H. van, Brett, M., Haldane, A., Río, J. F. del, Wiebe, M., Peterson, P., … Oliphant, T. E. (2020). Array programming with NumPy. Nature, 585(7825), 357–362. https://doi.org/10.1038/s41586-020-2649-2

Higgins, M., Femina, P. C. L., Weber, J., Geirsson, H., Ryan, G., & Wauthier, C. (2021). Strain Partitioning and Interseismic Fault Behavior Along the Caribbean-South American Transform Plate Boundary. Tectonics, 40(8). https://doi.org/10.1029/2021tc006740

Hornbach, M. J., Braudy, N., Briggs, R. W., Cormier, M., Davis, M. B., Diebold, J., Dieudonne, N., Douilly, R., Frohlich, C., Gulick, S. P. S., Johnson, H. E., Mann, P., McHugh, C. M., Ryan-Mishkin, K., Prentice, C. S., Seeber, L., Sorlien, C. C., Steckler, M. S., Symithe, S., … Templeton, J. A. (2010). High tsunami frequency as a result of combined strike-slip faulting and coastal landslides. Nature Geoscience, 3(11), 783–788. https://doi.org/10.1038/ngeo975

Horrillo, J., Knight, W., & Kowalik, Z. (2008). Kuril Islands tsunami of November 2006: 2. Impact at Crescent City by local enhancement. Journal of Geophysical Research Oceans, 113. https://doi.org/10.1029/2007jc004404

IOC-UNESCO (2014). User's Guide for the Pacific Tsunami Warning Center Enhanced Products. In IOC Technical Series. UNESCO.

IOC-UNESCO (2026a). Venezuela: Member State Profile. Tsunami Programme, ICG/CARIBE-EWS. https://tsunami.ioc.unesco.org/en/member-states/venezuela

IOC-UNESCO (2026b). CARIBE WAVE: Caribbean and Adjacent Regions Tsunami Exercise. Intergovernmental Oceanographic Commission of UNESCO. https://tsunami.ioc.unesco.org/en/caribewave

Kubota, T., Saito, T., Tsushima, H., Hino, R., Ohta, Y., Suzuki, S., & Inazu, D. (2021). Extracting Near-Field Seismograms From Ocean-Bottom Pressure Gauge Inside the Focal Area: Application to the 2011 Mw 9.1 Tohoku-Oki Earthquake. Geophysical Research Letters, 48(7). https://doi.org/10.1029/2020gl091664

Leonard, M. (2006). Analysis of tide gauge records from the December 2004 Indian Ocean tsunami. Geophysical Research Letters, 33(17). https://doi.org/10.1029/2006gl026552

Ley de Marinas y Actividades Conexas, Decreto con Rango, Valor y Fuerza de Ley publicado en Gaceta Oficial de la República Bolivariana de Venezuela (2014). https://faolex.fao.org/docs/pdf/ven148053.pdf

Leys, C., Ley, C., Klein, O., Bernard, P., & Licata, L. (2013). Detecting outliers: Do not use standard deviation around the mean, use absolute deviation around the median. Journal of Experimental Social Psychology, 49(4), 764–766. https://doi.org/10.1016/j.jesp.2013.03.013

Monserrat, S., Vilibić, I., & Rabinovich, A. B. (2006). Meteotsunamis: atmospherically induced destructive ocean waves in the tsunami frequency band. Natural Hazards and Earth System Sciences, 6(6), 1035–1051. https://doi.org/10.5194/nhess-6-1035-2006

Oropeza, J., & Audemard, F. A. (2016). Contribución al estudio de tsunamis y otras amenazas costeras en Venezuela. Revista Nuestro Sur: Historia, Memoria y Patrimonio, 9, 193–215. https://www.researchgate.net/publication/309783657_CONTRIBUCION_AL_ESTUDIO_DE_TSUNAMIS_Y_OTRAS_AMENAZAS_COSTERAS_EN_VENEZUELA

Palma, M., Audemard, F., & Romero, G. (2010). New focal mechanism solutions for Venezuela and neighbouring areas 2005-2008: importance of the National Seismological Network's density and distribution. Revista Técnica de la Facultad de Ingeniería Universidad del Zulia, 33(2), 108–121. https://doaj.org/article/a8ae2a2fa4a74fc5acec40ce91d56004

Pawlowicz, R., Beardsley, B., & Lentz, S. (2002). Classical tidal harmonic analysis including error estimates in MATLAB using T_TIDE. Computers & Geosciences, 28(8), 929–937. https://doi.org/10.1016/s0098-3004(02)00013-4

Pérez, O. J., Bilham, R., Bendick, R., Velandia, J., Hernández, N., Moncayo, C., Hoyer, M., & Kozuch, M. (2001). Velocity field across the Southern Caribbean Plate Boundary and estimates of Caribbean/South-American Plate Motion using GPS Geodesy 1994–2000. Geophysical Research Letters, 28(15), 2987–2990. https://doi.org/10.1029/2001gl013183

Pousse-Beltran, L., Vassallo, R., Audemard, F., Jouanne, F., Carcaillet, J., Pathier, E., & Volat, M. (2017). Pleistocene slip rates on the Boconó fault along the North Andean Block plate boundary, Venezuela. Tectonics, 36(7), 1207–1231. https://doi.org/10.1002/2016tc004305

Rabinovich, A. B. (1997). Spectral analysis of tsunami waves: Separation of source and topography effects. https://doi.org/10.1029/97jc00479

Rabinovich, A. B. (2009). Seiches and Harbor Oscillations. https://doi.org/10.1142/9789812819307_0009

Reinoza, C., Jouanne, F., Audemard, F., Schmitz, M., & Beck, C. (2015). Geodetic exploration of strain along the El Pilar Fault in northeastern Venezuela. Journal of Geophysical Research Solid Earth, 120(3), 1993–2013. https://doi.org/10.1002/2014jb011483

Roger, J., Pelletier, B., Duphil, M., Lefèvre, J., Aucan, J., Lebellegard, P., Thomas, B. E. O., Bachelier, C., & Varillon, D. (2021). The Mw 7.5 Tadine (Maré, Loyalty Islands) earthquake and related tsunami of 5 December 2018: seismotectonic context and numerical modeling. Natural Hazards and Earth System Sciences, 21(11), 3489–3508. https://doi.org/10.5194/nhess-21-3489-2021

Rusdin, A., Oshikawa, H., Divanesia, A. M. A., & Hatta, M. P. (2024). Analysis and Prediction of Tidal Measurement Data from Temporary Stations using the Least Squares Method. Civil Engineering Journal, 10(2), 384–403. https://doi.org/10.28991/cej-2024-010-02-03

Sahal, A., Roger, J., Allgeyer, S., Lemaire, B. J., Hébert, H., Schindelé, F., & Lavigne, F. (2009). The tsunami triggered by the 21 May 2003 Boumerdès-Zemmouri (Algeria) earthquake: field investigations on the French Mediterranean coast and tsunami modelling. Natural Hazards and Earth System Sciences, 9(6), 1823–1834. https://doi.org/10.5194/nhess-9-1823-2009

SHN, Servicio. de Hidrografía, Oceanografía, Meteorología y Cartografiado Náutico. (2024). Reporte Nacional de la República Bolivariana de Venezuela a la Comisión Hidrográfica Mesoamericana y del Mar Caribe. In 25th Meeting of the Meso American–Caribbean Sea Hydrographic Commission. International Hydrographic Organization. https://iho.int/uploads/user/Inter-Regional%20Coordination/RHC/MACHC/MACHC25/MACHC25_2024_06.15_SP_REPORTE_NACIONAL_Venezuela.pdf?utm_source=chatgpt.com

Tappin, D. R., Watts, P., & Grilli, S. T. (2008). The Papua New Guinea tsunami of 17 July 1998: Anatomy of a catastrophic event. Natural Hazards and Earth System Sciences, 8, 243–266. https://doi.org/10.5194/nhess-8-243-2008

Styron, R., & Pagani, M. (2020). The GEM Global Active Faults Database. Earthquake Spectra, 36, 160–180. https://doi.org/10.1177/8755293020944182

Tanioka, Y., & Satake, K. (1996). Tsunami generation by horizontal displacement of ocean bottom. Deep Blue (University of Michigan), 23(8), 861–864. https://doi.org/10.1029/96gl00736

Thomson, D. J. (1982). Spectrum estimation and harmonic analysis. Proceedings of the IEEE, 70(9), 1055–1096. https://doi.org/10.1109/proc.1982.12433

Torrence, C., & Compo, G. P. (1998). A Practical Guide to Wavelet Analysis. Bulletin of the American Meteorological Society, 79(1), 61–78. https://doi.org/10.1175/1520-0477(1998)079<0061:apgtwa>2.0.co;2

USGS (2026a). M 7.2 — 20 km E of San Felipe, Venezuela. Earthquake Hazards Program; United States Geological Survey (USGS). https://earthquake.usgs.gov/earthquakes/eventpage/us6000t7zc

USGS (2026b). M 7.5 — 20 km W of Catia La Mar, Venezuela. United States Geological Survey. https://earthquake.usgs.gov/earthquakes/eventpage/us6000t7zp

Virtanen, P., Gommers, R., Oliphant, T. E., Haberland, M., Reddy, T., Cournapeau, D., Burovski, E., Peterson, P., Weckesser, W., Bright, J., Walt, S. J. van der, Brett, M., Wilson, J., Millman, K. J., Mayorov, N., Nelson, A. R. J., Jones, E., Kern, R., Larson, E., … Pudlik, T. (2020). SciPy 1.0: fundamental algorithms for scientific computing in Python. Nature Methods, 17(3), 261–272. https://doi.org/10.1038/s41592-019-0686-2

Wang, Y., Zamora, N., Quiroz, M., Satake, K., & Cienfuegos, R. (2021). Tsunami Resonance Characterization in Japan Due to Trans-Pacific Sources: Response on the Bay and Continental Shelf. Journal of Geophysical Research Oceans, 126(6). https://doi.org/10.1029/2020jc017037

Weber, J., Dixon, T. H., DeMets, C., Ambeh, W. B., Jansma, P. E., Mattioli, G. S., Saleh, J., Sella, G., Bilham, R., & Pérez, O. J. (2001). GPS estimate of relative motion between the Caribbean and South American plates, and geologic implications for Trinidad and Venezuela. Geology, 29(1), 75. https://doi.org/10.1130/0091-7613(2001)029<0075:geormb>2.0.co;2

Supplementary Files

This is a list of supplementary files associated with this preprint. Click to download.

- SupplementaryMaterial.pdf